Tidal-induced mixing and diapycnal nutrient fluxes in the Mauritanian upwelling region

Jens Schafstall,[1] Marcus Dengler,[1] Peter Brandt,[1] and Hermann Bange[1]

Received 25 October 2009; revised 12 February 2010; accepted 8 April 2010; published 8 October 2010.

[1] The Mauritanian coastal area is one of the most biologically productive upwelling regions in the world ocean. Shipboard observations carried out during maximum upwelling season and short-term moored observations are used to investigate diapycnal mixing processes and to quantify diapycnal fluxes of nutrients. The observations indicate strong tide-topography interactions that are favored by near-critical angles occurring on large parts of the continental slope. Moored velocity observations reveal the existence of highly nonlinear internal waves and bores and levels of internal wave spectra are strongly elevated near the buoyancy frequency. Dissipation rates of turbulent kinetic energy at the slope and shelf determined from microstructure measurements in the upper 200 m averages to $\varepsilon = 5 \times 10^{-8}$ W kg^{-1}. Particularly elevated dissipation rates were found at the continental slope close to the shelf break, being enhanced by a factor of 100 to 1000 compared to dissipation rates farther offshore. Vertically integrated dissipation rates per unit volume are strongest at the upper continental slope reaching values of up to 30 mW m^{-2}. A comparison of fine-scale parameterizations of turbulent dissipation rates for shelf regions and the open ocean to the measured dissipation rates indicates deficiencies in reproducing the observations. Diapycnal nitrate fluxes above the continental slope at the base of the mixed layer yielding a mean value of 12×10^{-2} μmol m^{-2} s^{-1} are amongst the largest published to date. However, they seem to only represent a minor contribution (10% to 25%) to the net community production in the upwelling region.

Citation: Schafstall, J., M. Dengler, P. Brandt, and H. Bange (2010), Tidal-induced mixing and diapycnal nutrient fluxes in the Mauritanian upwelling region, *J. Geophys. Res.*, *115*, C10014, doi:10.1029/2009JC005940.

1. Introduction

[2] The coastal region off Mauritania is part of an eastern boundary upwelling system that extends from the northern tip of the Iberia peninsula at 43°N to south of Dakar at about 10°N. While between 20°N and 25°N upwelling is present throughout the year, upwelling strength to the north and to the south of these latitudes exhibits a pronounced seasonal cycle [*Barton et al.*, 1998]. This seasonal variability is due to changes in wind forcing associated with the migration of the Intertropical Convergence Zone. Upwelling favorable winds along the coast off Mauritania prevail primarily from December to April.

[3] The redistribution of nutrients, sediments, freshwater, and pollutants throughout the water column at the transition zone between the open ocean and the coastal region, in which several of these quantities enter the ocean from terrestrial sources, is of local and global importance [*Carter et al.*, 2005]. The hydrodynamics at the continental slope, however, are strongly influenced by the slope itself, which has consequences for mixing processes and transport. Interaction of the ocean with topographic boundaries accelerates an energy cascade from large-scale open ocean tides to the small turbulent scales [e.g., *Sandstrom and Oakey*, 1995]. In general, the first step of this energy cascade is the interaction of barotropic tidal flow with topography, leading to the generation of baroclinic motions in the presence of stratification. As described by linear theory, the interaction between barotropic tides and topography leads to the generation of internal waves with comparably long horizontal wavelengths (tens of kilometers), which are known as internal tides [e.g., *Baines*, 1982], while the inclusion of nonlinear and nonhydrostatic effects additionally allows generation of nonlinear internal waves with much shorter wavelengths (hundreds of meters) and high frequency (close to N) [e.g., *Legg and Adcroft*, 2003]. Observations from continental slopes showed internal tides becoming sufficiently nonlinear to form internal bores followed by groups of high-frequency nonlinear internal waves [e.g., *Duda et al.*, 2004; *Holloway and Merrifield*, 1999]. These nonlinear internal waves that are often highly energetic and have particularly large particle velocities can locally be the dominant factor for ocean mixing [*MacKinnon and Gregg*, 2003; *Moum and Nash*, 2000;

[1]Leibniz-Institut für Meereswissenschaften, IFM-GEOMAR, Kiel, Germany.

0148-0227/10/2009JC005940

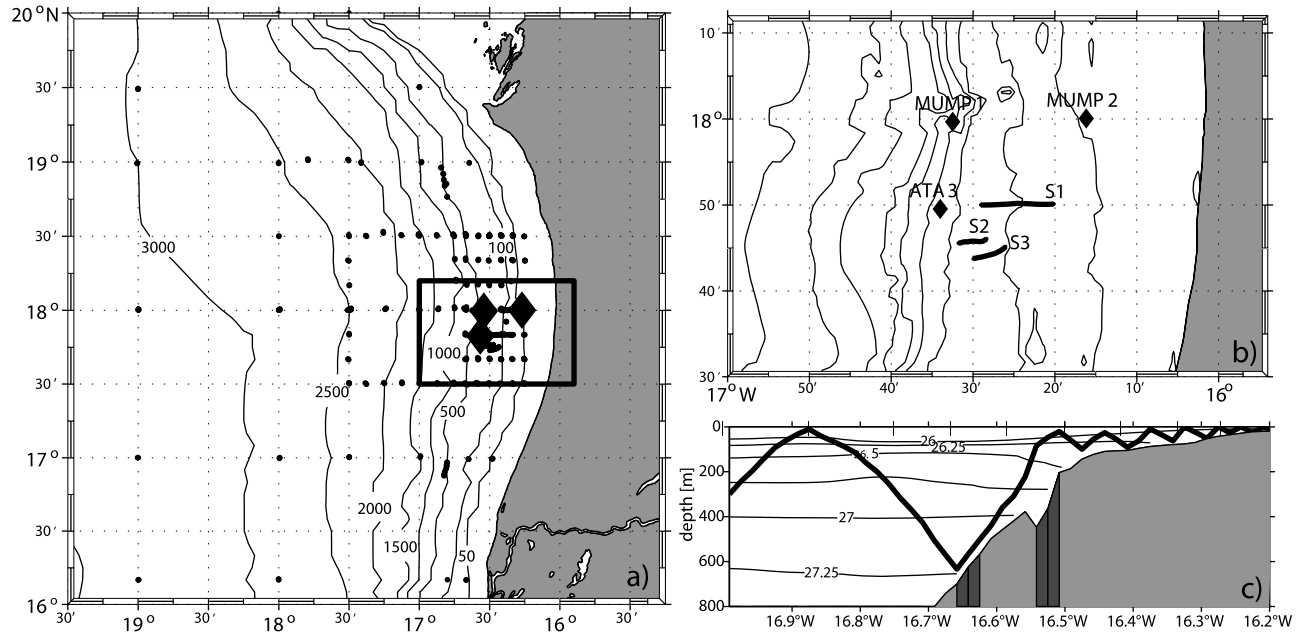

Figure 1. (a) Shows map of positions of individual microstructure stations (black dots) and moorings (diamonds). (b) Enlarged view of mooring positions and microstructure transects (S1, S2, and S3) discussed in section 3.2. (c) Shows representative bathymetric slope along 18°N. Arbitrary M_2 tidal beam following equation (2) is indicated by thick black line. Critical and super-critical slopes are indicated by dark grey, subcritical slopes are indicated by light grey shading.

Moum et al., 2003; *Pingree et al.*, 1986]. It is generally accepted that the scattering and the reflection of internal waves from sloping topography can promote mixing. At the critical frequency, where the characteristic slope of internal waves matches the bottom slope, internal wave energy is amplified upon reflection, which is favorable for shear instability and turbulence [e.g., *Eriksen*, 1982, 1998]. Recent numerical simulations of internal wave reflection at topography by *Legg and Adcroft* [2003] suggested that enhanced mixing occurs at a variety of near-critical topographic slopes regardless of their curvature due to the generation of nonlinear internal waves.

[4] In the present study, we investigate the distribution of diapycnal mixing in the upper ocean of the Mauritanian upwelling region. Our observations from the continental slope and the shelf region, while showing internal tides and internal bores consisting of individual internal waves, indicate strong mixing occurring near the shelf edge. High-resolution observations from moorings, shipboard velocity measurements, and microstructure profilers resolve details of the velocity and density fluctuations from bores propagating onslope with maximum velocity signals at middepth or near the bottom. Additionally, they allow quantification of diapycnal fluxes of nutrients for different regions within the upwelling system. Although mixing at the upper continental slope has long been recognized as an important mechanism for the nutrient supply to productive layers in coastal waters [e.g., *Sandstrom and Elliott*, 1984], quantitative estimates of diapycnal nutrient fluxes in those regions are sparse. However, robust estimates of diapycnal transport of nutrients are vital for validating biogeochemical models and carbon export estimates from the euphotic zone [e.g., *Gnanadesikan et al.*, 2002].

[5] This paper is organized as follows: section 2 describes the available data set. Observations of turbulent mixing and large amplitude tidally induced internal waves are presented in section 3. In section 4, the observations are used to assess skill of different fine-scale parameterizations of turbulence. Estimates of diapycnal nutrient fluxes are presented in section 5, while we conclude with a summary in section 6.

2. Data and Methods

2.1. Data

[6] Between July 2006 and February 2008, a physical and biogeochemical measurement program was carried out in the upwelling region off northwest Africa as part of the Mauritanian Upwelling and Mixing Process (MUMP) study and the Surface Ocean Processes in the Anthropocene (SOPRAN) project. Altogether, five cruises were carried out, four during maximum upwelling in January–March, and one cruise in summer when upwelling is lowest. The main goal of the observational program was to quantify physical and biogeochemical processes that contribute to variability of sea surface temperature and to emission of trace gases in the upwelling region.

[7] The data set presented here is a subset of the observations in the previous paragraph and consists of shipboard observations from three cruises carried out in January (FS Poseidon cruise P347) and February 2007 (FS Poseidon cruise P348) and in February 2008 (N/O L'Atalante, IFM-GEOMAR cruise 3). Additionally, velocity as well as temperature and salinity time series were obtained from short-term mooring deployments of 10–12 day durations from different positions along the continental slope (Figure 1). Shipboard observations included microstructure

Table 1. Mooring Instrumentation and Setup

	Instrument	Serial No.	Variables	Depth (m)	Sampling Rate
MUMP 1[a]	Mini T	3388	t, p	25	300 s
	Moored profiler	RO1 (JT)	Profiles of u, v, w, p, t, c	40–380	30 min/profile
	Microcat	2249	t, c	385	180 s
	Argonaut	179	u, v	386	180 s
MUMP 2[b]	ADCP (1200 kHz)	001	Profiles of u, v, w	12–32	2 s (10 subpings, mode 12)
	Mini T	56	t, p	35	300 s
	Microcat	2251	t, c	36	180 s
Ata 3[c]	ADCP (1200 kHz)	001	Profiles of u, v, w	205–220	2 s (10 subpings, mode 12)
	ADCP (300 kHz)	001	Profiles of u, v, w	200–50	5 s
	Microcat	1316	t, c	204	5 s
	Microcat	1317	t, c	225	5 s
	Microcat	1318	t, c	235	5 s
	Microcat	1321	t, c	245	5 s

[a]Latitude, 17°59.65′N; longitude, 16°32.00′W°; water depth, 386 m; start, 22 January 2007 1026 UT; stop, 2 January 2007 1315 UT.
[b]Latitude, 18°00.08′N; longitude, 16°16.15′W°; water depth, 38 m; start, 22 January 2007 1628 UT; stop, 2 January 2007 0820 UT.
[c]Latitude, 17°50.00′N; longitude, 16°34.00′W°; water depth: 264 m; start, 5 February 2008 1000 UT; stop, 16 February 2008 1020 UT.

shear and temperature profiles, continuous velocity measurements by vessel-mounted acoustic Doppler current profilers (VMADCPs) and conductivity-temperature-depth-oxygen (CTD-O_2) profiles. Furthermore, water samples from Niskin bottles were taken from different depths and analyzed for salinity, oxygen, nutrients, and other biogeochemical parameters.

[8] Microstructure data were collected using different loosely tethered microstructure profilers (MSS90L and MSS90D) manufactured by Sea & Sun Technology in cooperation with ISW-Wassermesstechnik. All profilers were equipped with two shear sensors (airfoil), a fast temperature sensor (FP07), an acceleration sensor, tilt sensors, and standard CTD sensors. In addition, an optical turbidity probe and an oxygen sensor (Oxygardt) were mounted to the profiler used during the February 2008 cruise. A detailed description of the instruments is given in *Prandke and Stips* [1998]. The profilers were adjusted to decent at 0.5–0.6 ms^{-1}. High-frequency shear fluctuations measured by airfoils can be used to estimate the local dissipation rate of turbulent kinetic energy (ε) (see section 2.2). Noise levels of turbulent dissipation rates from the microstructure profilers are better than 1×10^{-9} W kg^{-1} for the MSS90L and better than 4×10^{-10} W kg^{-1} for MSS90D.

[9] The microstructure sampling strategy chosen was a compromise between temporal and spatial resolution. Microstructure profiles were collected at about 160 stations during the 3 cruises encompassing the region from 16°N to 20°N and from the Cape Verde islands to the Mauritanian coast (Figure 1). At each station, three to eight repeated microstructure profiles were recorded. Maximum sampling depths were about 250 m or the bottom in shallower waters. In addition to individual stations, several microstructure transects were sampled by continuous profiling along a section while steaming at about 1.5 knots. The exact location of three of those yo-yo transects discussed in the present study are depicted in Figure 1.

[10] During most of the microstructure stations, additional CTD-O_2 profiles and water samples were collected using a Seabird 911 system attached to a rosette of 12 (FS Poseidon) or 24 (N/O L'Atalante) Niskin bottles. Water samples were used for calibration purposes as well as for analysis of biogeochemical parameters including nutrients. Water samples for calibration of Seabird conductivity sensors were analyzed on board using Guildline salinometers. Final accuracy of salinity derived from CTD measurements was in general better than 0.003.

[11] On all cruises, continuous velocity data were recorded by VMADCPs. On FS Poseidon, an RDI-Ocean Surveyor (75 kHz) was available that was configured to record data at a pingrate of 2.4 s using 100 bins and a bin length of 8 m. On N/O L'Atalante, a 75 kHz broadband acoustic Doppler current profiler (ADCP) and a 300 kHz ADCP were simultaneously collecting data. Bin size was 16 and 4 m, respectively. Standard techniques [e.g., *Fischer et al.*, 2003] were used during data postprocessing.

[12] In addition to the shipboard observations, velocity and CTD time series from three short-term mooring deployments are available (Table 1). Two moorings were deployed on the continental slope in a water depth of 385 and 265 m while a third mooring was deployed on the shelf in a depth of 38 m (Figure 1). The deeper mooring on the continental slope was equipped with a McLane moored profiler (MMP) set to climb the depth range from 40 to 380 m every 30 min. The MMP records 3-D velocity and CTD data while climbing up and down the mooring cable. The shallower mooring consisted of an upward-looking 300 kHz ADCP, a downward-looking 1200 kHz ADCP, and a few CTD and temperature and depth (TD) loggers below and above the ADCPs. The ADCPs were configured to ping every 5 s using a bin size of 4 m (300 kHz) and every 2 s with 10 subpings (mode 12) using a bin size of 0.5 m (1200 kHz). The mooring on the shelf was deployed in a water depth of 38 m. It was equipped with a 1200 kHz ADCP (Table 1) that used the same configuration as the 1200 kHz ADCP used on the continental shelf.

2.2. Dissipation Rate and Turbulent Eddy Diffusivity Calculation

[13] From velocity shear measurements by airfoil probes, the rate of turbulent kinetic energy dissipation (ε) can be estimated [e.g., *Gregg*, 1999; *Lueck et al.*, 2002; *Oakey*, 1982; *Osborn*, 1974, 1980]. Here, the variance method was used to calculate dissipation rates: Wave number spectra were calculated from 1 s ensembles of shear data (1024 individual measurements), which corresponds to a vertical

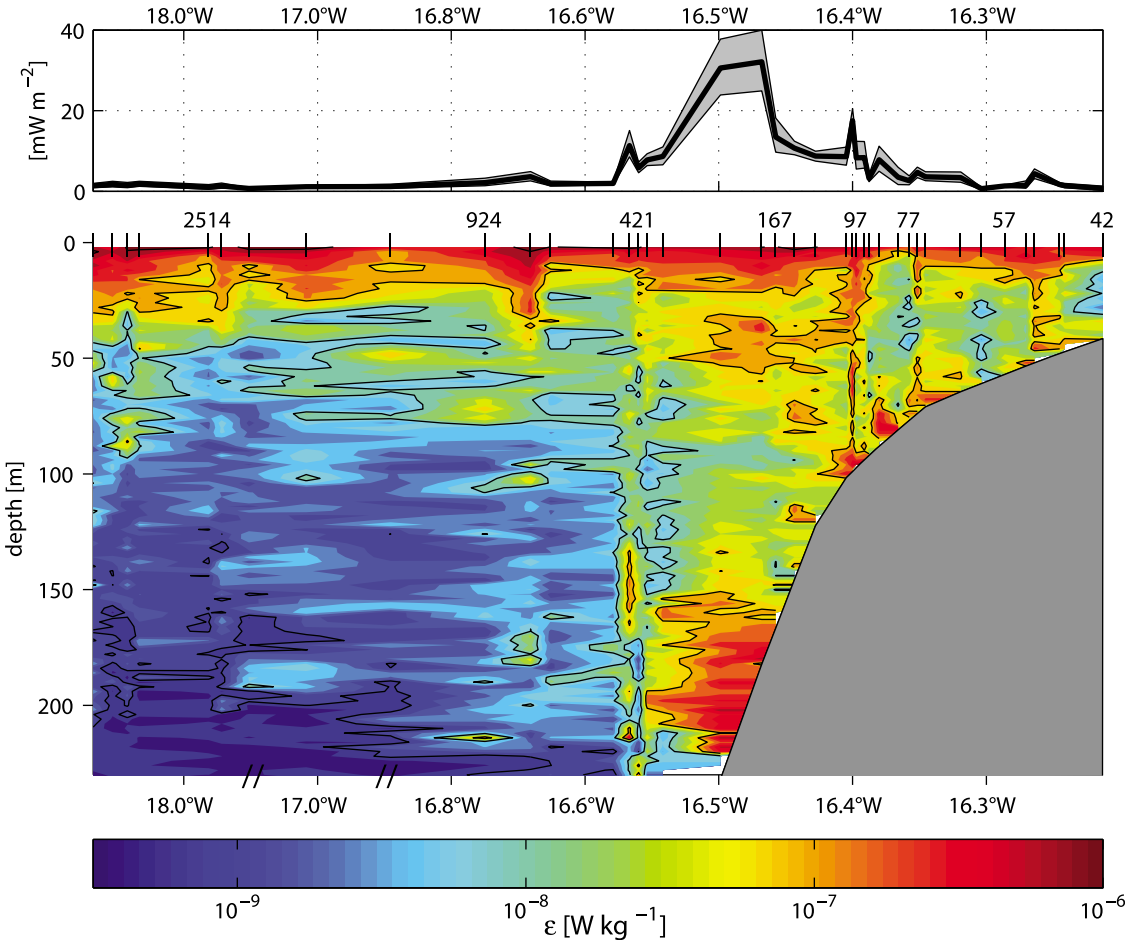

Figure 2. Upper panel: Vertically integrated dissipation rates from below the mixed layer to 220m or the bottom against longitude. Grey shading indicates 95% confidence intervals (from bootstrap). Lower panel: Longitude-depth distribution of dissipations rates of turbulent kinetic energy from all profiles collected during winter upwelling season. Data are binned in groups of 20 profiles as indicated by ticks on top of panel where numbers indicate water depth.

interval of 0.5–0.6 m. Estimates of ε are then derived by integrating the shear spectrum using the relationship for isotropic turbulence

$$\varepsilon = 7.5\mu\overline{\left(\frac{\partial u}{\partial z}\right)^2} = 7.5\mu\left(\int_{k_{\min}}^{k_{\max}} E_{du'/dz}(k)dk\right), \qquad (1)$$

where μ is the dynamic viscosity of seawater and $E_{du'/dz}$ (k) the shear wave number spectrum. We obtained shear variance by integrating the shear wave number spectrum from a lower wave number, $k_{\min}$ (taken as 3 cpm), to an upper cutoff number $k_{\max}$, which is dependent on the Kolmogorow wave number. The upper cutoff was varied by iteration between a maximum value of 30 cpm and a minimum value of 14 cpm when dissipation is low, similar to the procedure described in [*Moum et al.*, 1995]. The loss of variance due to incomplete integration was compensated by extrapolating the observed spectrum in the neglected wave number band using the theoretical Nasmyth spectrum [*Nasmyth*, 1970]. Similarly, loss of variance resulting from spatial averaging due to the finite size of the sensor tip was corrected following the work of *Prandke et al.* [2000]. Calculations of ε for each of the two shear sensors were done separately. Before individual estimates were merged, the derived ε values for each sensor were carefully edited for outliers that predominately originate from collisions of the sensors with small particles. Dissipation rates from the first 5 m below the surface are often contaminated by ship-induced turbulence and are therefore excluded from the analysis. Turbulent eddy diffusivities (K_ρ) were calculated from ε and the buoyancy frequency (N), as $K_\rho = \Gamma\varepsilon/N^2$ [*Osborn*, 1980]. Mixing efficiency, Γ, was set to 0.2 [*Oakey*, 1982].

3. Observations

[14] The microstructure observations available from the measurement campaign (Figure 1) span a wide region within the Mauritanian upwelling system. Repeated profiles were collected from 16°N to 20°N and from 25°W to the coast. Water depth in this region ranges from 3000 m in the west to less than 30 m close to the coast. A composite of the distribution of averaged dissipation rates against bottom depth best illustrates the dependence of strength of turbulence on the different topographic environments (Figure 2). In this composite, each microstructure cast from south of 19°N is projected according to water depth on an arbitrary zonal

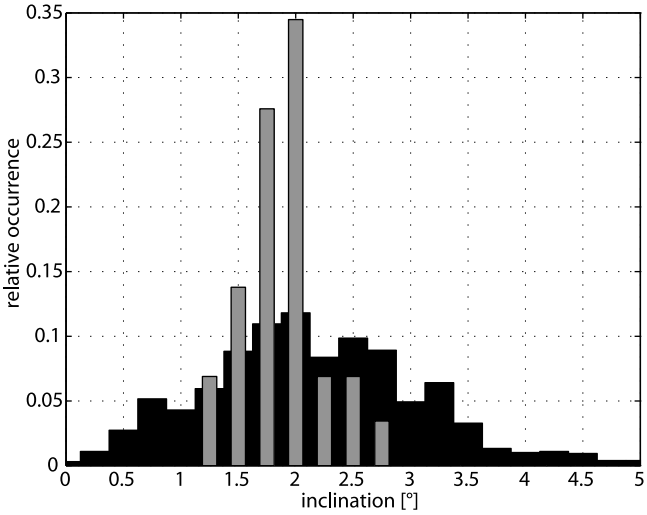

Figure 3. Relative occurrence of topographic slope angles (black) and angles of the semidiurnal internal tide characteristics (gray) between 16.5°N and 19.5°N at the upper Mauritanian continental slope (200 and 600 m depth).

section for which we used an idealized bathymetry along 18°N. Dissipation rates from 20 topographically adjacent profiles were arithmetically averaged on depth levels and contoured.

[15] Away from the shelf region and the continental slope, turbulent dissipation rates and thus diapycnal mixing below the surface layer are lower than 10^{-9} W kg^{-1} (Figure 2). Here, only a few individual profiles showed elevated levels of turbulence. As diagnosed from simultaneously measured shipboard ADCP and CTD data (not shown), these elevated levels were often associated with baroclinic near-inertial waves. In contrast, the observations from the continental slope indicate strongly enhanced levels of turbulence, predominately close to the bottom and at middepth. Average dissipation rates inshore from 16.6°W, corresponding to bottom depths shallower than 450 m, exceed values of 10^{-8} W kg^{-1} almost everywhere while maxima are larger than 10^{-7} W kg^{-1}. In fact, the mean dissipation rate for depth larger than 30 m and inshore of the 450 m isobaths yields 4.9×10^{-8} W kg^{-1}. The middepth maximum (40 to 90 m) between 16.55°W and 16.4°W (Figure 2), having average dissipation rates $\varepsilon > 10^{-7}$ W kg^{-1}, was determined from more than 200 microstructure profiles from this region and thus marks a robust feature. Inshore from the shelf break, dissipation rates are also enhanced, but on average somewhat weaker than along the continental slope. In addition, the water column above the shelf is only weakly stratified. Elevated levels of ε in the mixed layer above 30 m depth are due to wind and nighttime convection and will not be discussed further.

[16] Accordingly, vertically integrated dissipation rates calculated from the maximal sampling depth (220 m or the seafloor in shallower waters) to the base of the mixed layer are strongly enhanced at the continental slope (Figure 2, upper panel). The integrated dissipation rate can be interpreted as the kinetic and potential energy extracted by turbulence from the background velocity and density fields. Background fields here indicate mean and variability caused by all other processes except turbulence. Close to the shelf break, integrated dissipation peaks at about 30 mW m^{-2} and the mean value for the approximately 20 km wide strip between the 450 and 95 m isobaths yields 13 mW m^{-2}. This average value is on the higher end of similar estimates from continental slopes in other oceanic regions [e.g., *Sherwin*, 1988; *Inall et al.*, 2000; *Sharples et al.*, 2001a], indicating that turbulence production at the Mauritanian continental slope is somewhat increased compared to other continental slope regions.

[17] It should be noted that during high upwelling season, when the data was collected, the near-surface isopycnals slope upward toward the coast, whereas isopycnals slope downward at depths below 150 m, resulting in a reduced stratification at the upper continental slope (Figure 1c). In the following section, we focus on observations of oceanic processes that lead to enhanced turbulence at the continental slope off Mauritania below the mixed layer.

3.1. Internal Waves at the Continental Slope

[18] Barotropic or low vertical mode baroclinic tidal currents passing topographic features such as mid-ocean ridges or continental slopes can efficiently generate internal tides of small vertical scale [e.g., *Gerkema and Zimmerman*, 1995]. This mechanism is particularly effective when the slope of topography matches the slope of the linear internal tide characteristic, s (i.e., the path of the group velocity vector), which is given by:

$$s^2 = \left(\frac{\sigma^2 - f^2}{N^2 - \sigma^2}\right), \tag{2}$$

where f is the inertial frequency, σ is the frequency of the internal tide, and $N(z)$ the local buoyancy frequency as a function of depth. Topographic slopes are classified as supercritical, critical, or subcritical when they are greater than, equal to, or less than the internal wave slope, respectively [e.g., *Holloway*, 1985]. Upon reflection, internal waves preserve their angle to the horizontal rather than to the reflecting surface [*Phillips*, 1977], so that reflection from slopes near the critical angle leads to reflected waves with higher wave numbers and greater shear [e.g., *Eriksen*, 1982, 1985]. When the horizontal velocity of the wave approaches the wave phase speed, nonlinear processes need to be considered. Transformation of the wave into an internal bore, a series of distinct high-frequency waves, or wave trains having smaller wavelength may occur. The propagation of these nonlinear waves is almost horizontal while following isopycnals instead of characteristic lines.

[19] The upper continental slope off Mauritania is, for the observed stratification, frequently near-critical or critical for the M_2 frequency (Figures 1c and 3). In fact, about 90% of the topographic inclinations derived from the 1° resolution topography by *Smith and Sandwell* [1997] for the upper continental slope (200–600 m) off Mauritania (16.5°N–19.5°N) are between 0.5° to 3.5° (Figure 3). The angles of internal tide characteristics, calculated using equation (2) from all CTD profiles observed within the corresponding area, vary between 1° and 3° (for each profile an averaged N over the lower 100 m was used). As both probability distributions (Figure 3) peak at an angle of 2°, near critical reflection at the upper continental slope is likely.

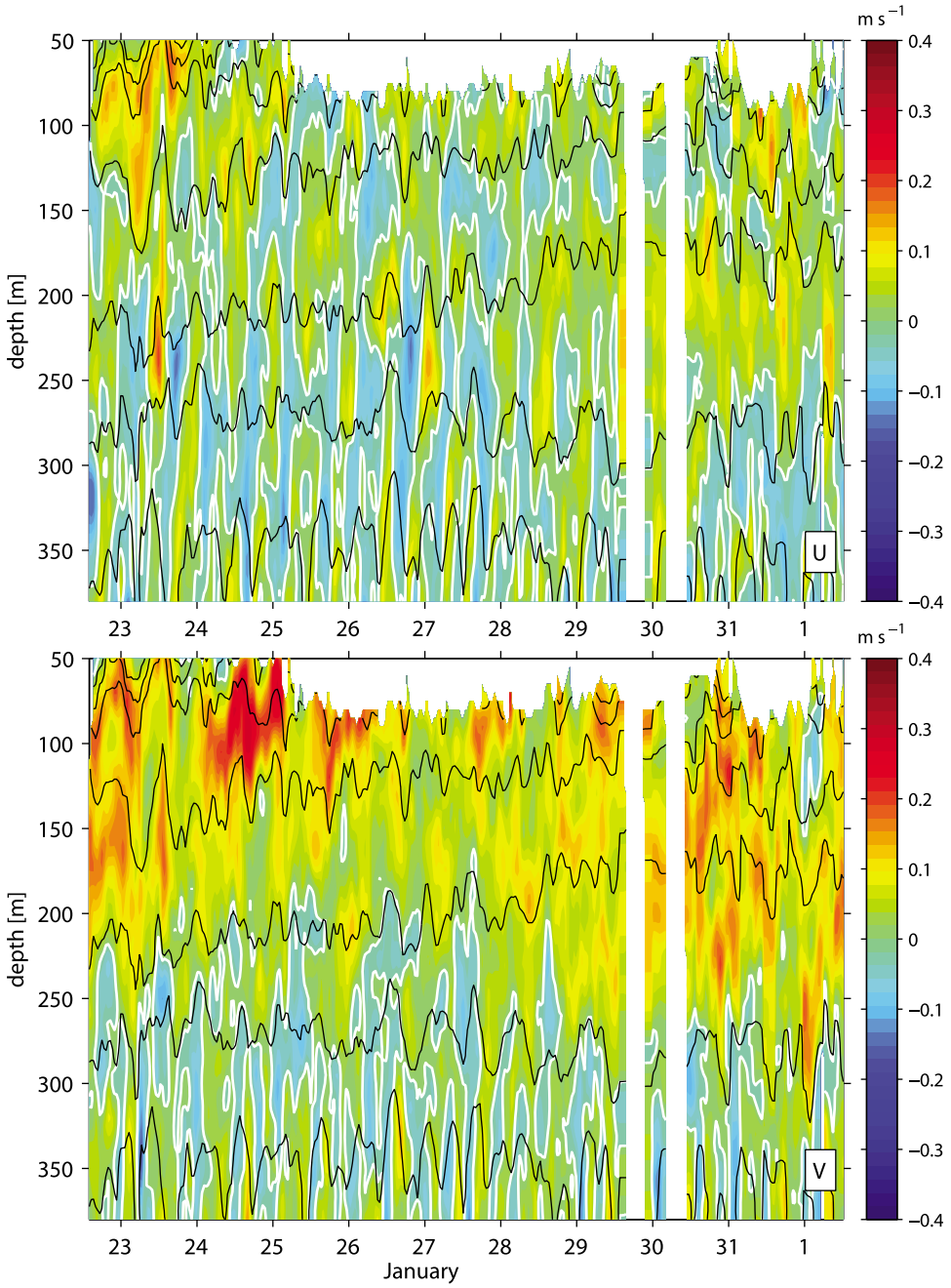

Figure 4. Time series of zonal (cross-slope, upper panel) and meridional (along-slope, lower panel) velocity profiles collected by the moored profiler deployed at 386 m depth. Zero isotachs are represented by while contours. Variability of isotherms (black contours) indicates associated vertical displacements.

[20] Limitations in temporal and spatial data coverage do not allow a complete description of the internal tide evolution, including their offshore generation, shoreward propagation, possible disintegration into higher frequency waves, and finally dissipation over the outer continental shelf. Nevertheless, our observations from the upper Mauritanian continental slope captured some of these processes. A 10 day velocity time series recorded by a moored profiler (Table 1) deployed at the continental slope at about 400 m depth shows the presence of semidiurnal tides (Figure 4). Although the record is too short to permit a detailed tidal analysis, a rough estimate of the tidal amplitude was obtained by fitting a harmonic of M_2 frequency to the time series. The results indicate that the M_2 tide accounts for less than 10% of the total variance and has amplitudes varying considerably with depth of about 0.01–0.025 m s^{-1} in the along-slope component and 0.025–0.04 m s^{-1} in the cross-slope component.

[21] During several occasions (e.g., at noon on 23 January and in the early morning on 27 January in Figure 4), particularly energetic baroclinic flows with vertical scales of

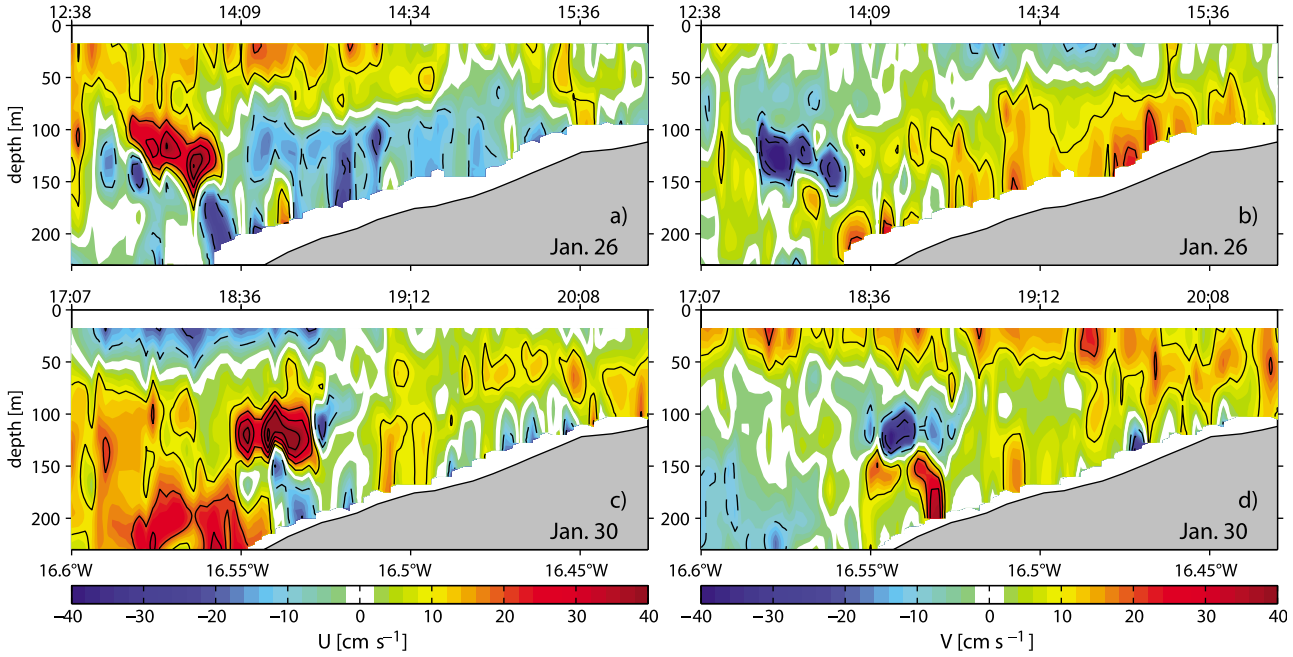

Figure 5. Zonal sections of (a, c) zonal (cross-slope) and (b, d) meridional (along-slope) velocity profiles collected by vessel-mounted acoustic Doppler current profilers (VMADCPs) along 17°50′N (black contour intervals are 0.1 m s^{-1}).

about 50 m were found between 175 and 275 m depths. Velocities within these events, which are likely of tidal origin, were of the order of 0.3 m s^{-1}, much stronger than the harmonic semidiurnal velocity component. Because of the low sampling frequency of the moored profiler, detailed characterization of these signals is not possible. It should be noted that short-term isopycnal displacements of less than 1 day determined from CTD data of the moored profiler were strongly pronounced with mean peak-to-through amplitudes of about 30 m in upper layers (50–150 m) and 70 m at middepth (about 300 m).

[22] Some of the cross-slope VMADCP velocity sections show the presence of very strong cross-slope and along-slope velocity signals of short horizontal (2–3 km) and vertical scales (50–80 m; Figure 5). Velocities within these features that are strongest at middepth, in a water depth between 75 and 175 m (Figure 5) exceeded 0.4 m s^{-1} in onslope and 0.3 m s^{-1} in southerly direction. At their shoreward side, the horizontal flow is strongly convergent, typical for internal bores. Within an individual feature, several velocity maxima are distinguishable.

[23] Similar bores were observed in velocity time series (Figure 6) from ADCPs that were moored at a water depth of 265 m (Table 1). This mooring was situated somewhat inshore of the moored profiler discussed in the previous paragraph. (Figure 1b), but on the same latitude as the velocity sections shown in Figure 5. The 11 day time series shows strong velocity maxima of 1 to 5 hour duration occurring at varying depth in the water column. Velocities within the features frequently exceed 0.3–0.4 m s^{-1} and their vertical extent is between 50 and 100 m. The bores that exhibit predominately onshore and southward velocities are associated with temperature changes of 1°C to 2°C and density changes of 0.2–0.5 kg m^{-3} at a depth of 205 m, 60 m above the seafloor (Figure 6). Apparently, the occurrence of these bores did not correspond to the same phase of the M_2 cycle, but in general two bores were observed during a 24 h period (Table 2). As indicated in Figure 6, 14 bores were identified from the current record (Table 2) having maximum velocity signals at middepth (11) or near the bottom (3). All events propagate in onslope direction, but there are large differences in the structure of the individual bores (Figures 7 and 8).

[24] Figure 7 shows two examples of bores having maximum velocity signals at middepth. Before passing the mooring, a downward shift of the isotherms indicated by a temperature increase of about 1°C at 205 m depth and by strong negative vertical velocities (Figures 7c and 7f) was observed. Associated with the lowering of the isopycnals, the layer of positive onshore flow deepens, indicating onshore propagation. Within the bores, several pulse-like onslope southward and vertical velocity events are detectable (Figure 7). Individual waves within the bore have associated time scales of 10–40 min. Temperature records are in good agreement with vertical velocity observations, indicating an alternating upward and downward shift of the isopycnals during the passing of individual waves. The existence of single pulses within the bore suggests a dispersive character. Nonlinear and nonhydrostatic effects act to transform the shoreward propagating bore into a sequence of individual internal waves typically arranged by amplitude [*Apel*, 2003].

[25] For bores with near bottom-intensified velocities (Figure 8, 0715–0815 UT), onshore propagation is indicated by the upward shift of isopycnals preceding the arrival of individual pulses, typical for internal waves of elevation. These bottom-intensified bores have stronger vertical velocities and individual waves within the bores have shorter time scales. A single wave passes the mooring site within

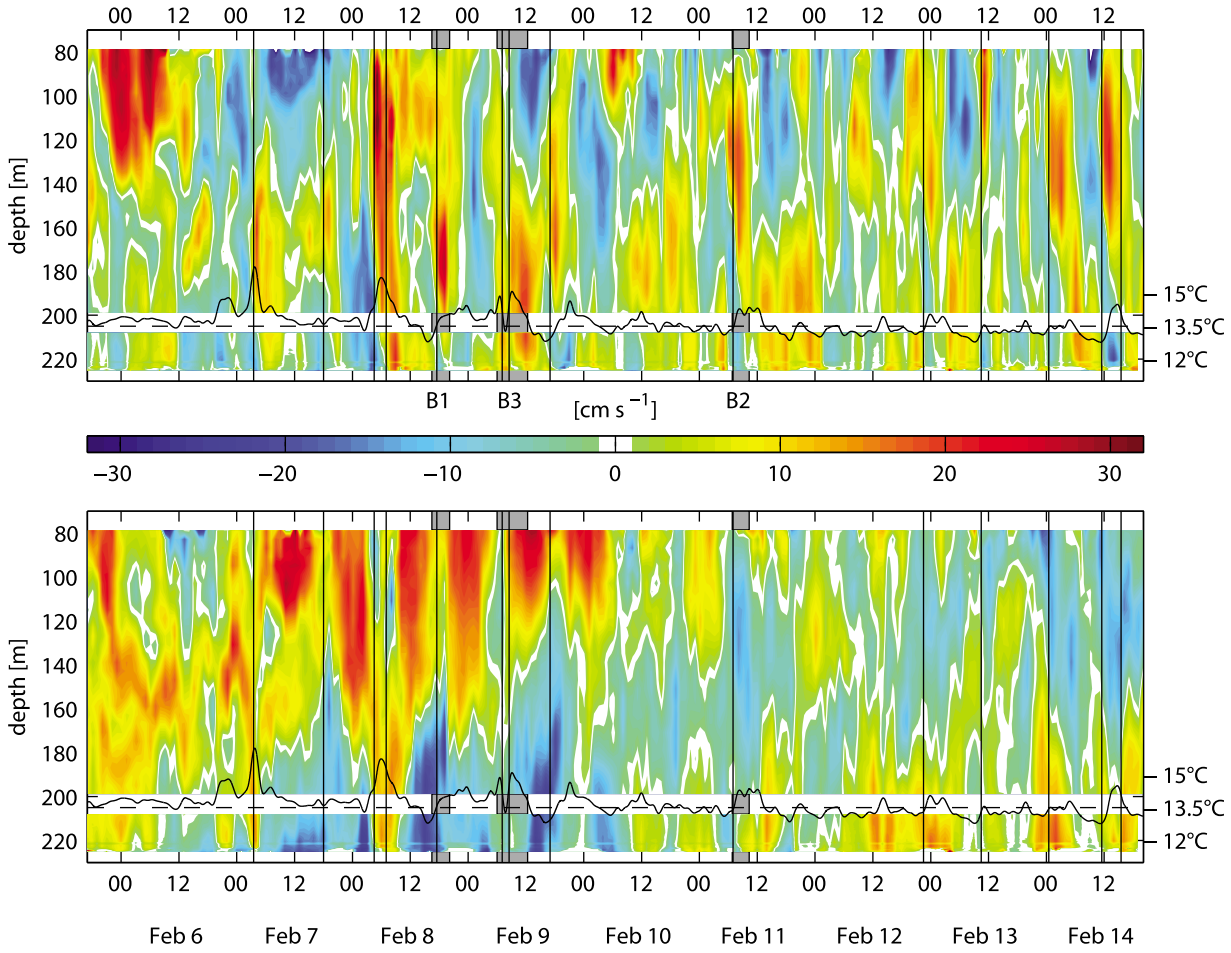

Figure 6. Time series of zonal (cross-slope, upper panel) and meridional (along-slope, lower panel) velocities (color contours) and temperature from 205 m depth (thick black line). Black vertical lines mark the appearance of individual bores listed in Table 2. Gray shaded areas (B1–B3) indicate time series shown in Figure 7 (B1 and B2) and Figure 8 (B3).

10–15 min, indicating wave frequencies close to the local buoyancy frequency (N).

[26] Possible explanations for the observed large differences between individual bores as well as their irregular occurrence with respect to the tidal cycle are (1) variable generation sites along the continental slope resulting in varying local propagation directions and different stages of their evolution, (2) variable stratification affecting baroclinic structure and propagation speed, and (3) highly nonlinear behavior including wave-topography interaction and internal wave breaking. It should be noted that the presence of the bores leads to strong vertical shear of horizontal velocity, particularly in the region below the bores.

[27] Because of the presence of internal bores consisting of individual waves at the continental slope, buoyancy-scaled spectra of horizontal velocity are strongly elevated at higher frequency (Figure 9). While for near-inertial frequencies, the open ocean internal wave spectrum (Garrett and Munk spectrum (GM); *Munk* [1981]) and observed spectra at the continental slope have similar levels, levels of observed spectra at higher frequencies are strongly elevated. Instead of an ω^{-2} frequency dependence that is typical for open ocean spectra, the frequency spectra from the continental slope exhibit an ω^{-1} dependence for frequencies between semidiurnal tidal frequency and about 1 cph. For even higher frequencies the continental slope spectra begin to flatten, leading to a broad peak near the buoyancy frequency. Here, spectral levels are two orders of magnitudes higher than GM. Contrary, the frequency spectrum calcu-

Table 2. Bore Parameter

Time (UT)	Vertical Extent (m)	Duration (min)	U_{max}/V_{max}
7 Feb 0330	120–200	~90	30/–15 cm s^{-1}
07 Feb 1800	120–180	~90	30/–25 cm s^{-1}
08 Feb 0430	80–200	~240	40/–15 cm s^{-1}
08 Feb 0700	>160	~75	20/–10 cm s^{-1}
08 Feb 1730	130–210	~160	30/–20 cm s^{-1}
09 Feb 0700	>160	~65	25/–15 cm s^{-1}
09 Feb 0830	100–210	~120	30/+15 cm s^{-1}
09 Feb 1700	100–200	~120	30/–25 cm s^{-1}
11 Feb 0700	80–180	~180	25/–15 cm s^{-1}
12 Feb 2230	<80–160	~120	35/–10 cm s^{-1}
13 Feb 1030	<80–140	~80	35/–15 cm s^{-1}
14 Feb 0030	80–170	~180	35/–20 cm s^{-1}
14 Feb 1130	80–180	~240	40/–15 cm s^{-1}
14 Feb 1530	>150	~70	10/+10 cm s^{-1}

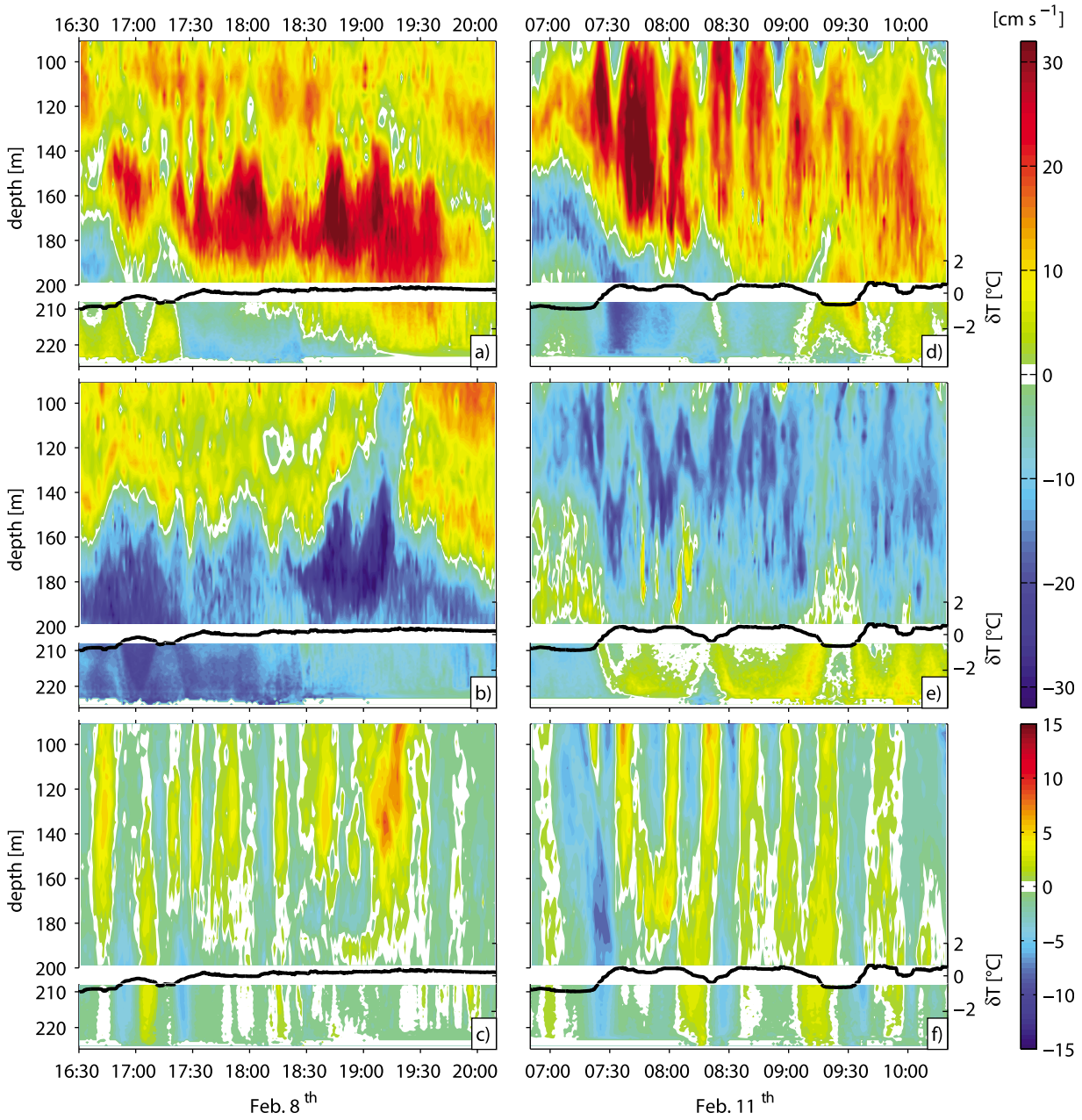

Figure 7. Time series of 1 min averages of (a, d) zonal, (b, e) meridional, and (c, f) vertical velocities (color contours) and temperature anomalies at 205 m depth (black tick line), see Figure 6 for details. Data from the down-looking 1200 kHz ADCP (208 and 225 m) are contoured using a reduced vertical scale.

lated from a velocity time series acquired by a 1200 kHz ADCP moored on the Mauritanian shelf close to the coast in a water depth of 38 m about 30 km onshore (see Table 1) do not show comparable elevated spectral levels at higher frequencies (Figure 9). Moreover, this frequency spectrum is very similar to the GM except for frequencies larger than about 1 cph, where it is slightly increased relative to the GM. Accordingly, the velocity time series from the shelf only occasionally indicate the presence of bores (not shown). When present, the features had reduced amplitudes of individual waves (0.05–0.15 m s^{-1}) in comparison to the bores on the continental slope.

[28] It should be stated that the 10 to 11 day time series from the shelf (38 m water depth) and the continental slope (265 m water depth) used in the spectral calculations were not recorded simultaneously. While both records are from the same month (February), they are from different years (2007 and 2008). The shipboard data (e.g., VMADCP, CTD) collected during mooring deployments and recoveries at the continental slope and on the shelf do not indicate large differences in the velocity variability and stratification

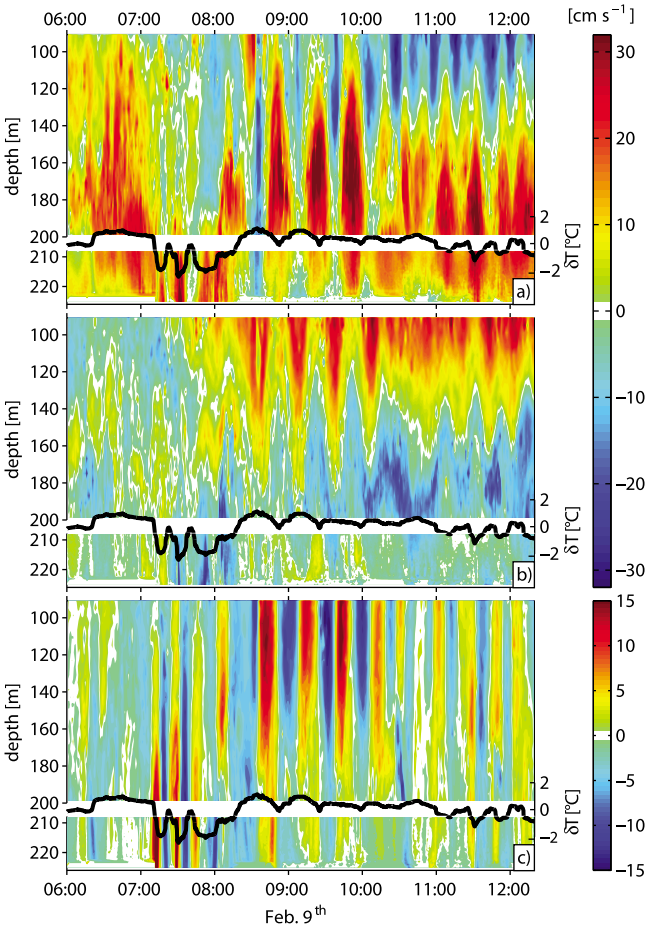

Figure 8. Same as Figure 7 except for a ~6 h period on 9 February 2008 (B3 in Figure 6).

during February of both years. We thus assume that the year-to-year variability was small and does not significantly affect the observed differences between spectra from the continental slope and the shelf.

[29] Because velocity variance on the shelf close to the coast is not particularly elevated, the bores and high-frequency waves observed in a water depth of 265 m either reflect or dissipate on the continental slope, thereby transferring their energy to turbulence. The enhanced average dissipation rate of turbulent kinetic energy observed at the continental slope (Figure 2) certainly supports that a large part of velocity variance at the continental slope is locally dissipated, presumably due to shoaling and wave breaking.

3.2. Stratification and Microstructure Transects Across the Continental Slope

[30] Several transects across the continental slope and the shelf break were conducted during the different cruises that included continuous velocity and backscatter measurements by shipboard ADCPs and yo-yo-CTD and microstructure profiling (Figure 1b). During the different transects (Figures 10–12), which are spatially as well as temporally separated from each other, observed dissipation rates vary by four orders of magnitude from the noise level (about 4×10^{-10} W kg^{-1}) to above 1×10^{-6} W kg^{-1}. Largest dissipation rates were found in the surface mixed layer and close to the bottom. A distinct feature common to these transects was a band of low stratification occurring parallel to the continental slope at depth between about 20 and 50 m above the bottom (Figures 10b and 11b). Such low stratification could be the result of enhanced mixing or of enhanced strain due to internal tides and waves. However, the latter mechanism seems to be unlikely as the low-stratification band was frequently observed in the available transects. The bands of low stratification are often accompanied by enhanced dissipation rates. This is particularly pronounced in the S2 transect (Figure 11) where elevated dissipation rates ($>1 \times 10^{-7}$ W kg^{-1}) frequently occur within the band above the slope. Turbulent diffusivities (K_ρ) in this region reach large values of 10^{-3} to 10^{-2} m^2 s^{-1}. Similar low-stratification bands above the slope were identified in nonhydrostatic model simulations of tide-topography interactions at critical slopes [*Legg and Adcroft*, 2003]. In their model, the low-stratification layers were caused by enhanced mixing occurring in onslope propagating bores.

[31] The dissipation rate below the surface mixed layer and above the bottom boundary layer is very variable because of different processes associated with tidally induced internal wave dynamics. Dissipation rates locally exceed values of 5×10^{-7} W kg^{-1} (Figures 10a, 11a, and 12a). Although many maxima in dissipation rate do not directly relate to resolved features in velocity or backscatter amplitude, a few events that are coherent in the data sets are noteworthy. In the near surface layer of transect S1 (Figure 10c, shortly before midnight), zonal velocity reveals an internal wave packet propagating onshore above the shelf. The vertical excursions of the isopycnals associated with the individual internal waves of the packet are also indicated but less resolved (Figure 10b). The leading wave of the internal wave packet with strongest onshore velocity component and deepest expression down to a depth of about 50 m is related to maximum dissipation rate (Figure 10a). Using yo-yo-MSS profiling, high-frequency internal waves can hardly be resolved. While strong undulations of the isopycnals are visible in the shallower part of transect S2 (Figure 11), a much better representation of the near-surface internal wavefield is given by the comparable high-resolution acoustic backscatter strength of the VMADCP (Figure 11d). Thus individual spike-like maxima in the dissipation rate cannot always be associated to individual internal wave events.

[32] During several transects an additional optical turbidity sensor attached to the MSS profiler were used. At the beginning of the section S3 at 2120 UT in Figure 12, near-bottom maxima in the dissipation rate and in the turbidity are coincidental with the passage of a near-bottom intensified wave of elevation, represented by a strong upward shift of the isotherms of around 30–40 m. This highly turbulent wave leads to a strong increase of suspended sediments in the bottom layer. Up to a height of 50 m above the seafloor, the dissipation rates are enhanced by a factor of 10 to 100 compared to surrounding values. Resuspended bottom sediments are also strongly enhanced nearly up to the same height. A similar situation was described by *Klymak and Moum* [2003] on the Oregon shelf; they found elevated 880 nm optical backscatter corresponding to resuspended fine silt and clay within an internal wave train. In addition, *Hosegood et al.* [2004] demonstrated the importance of

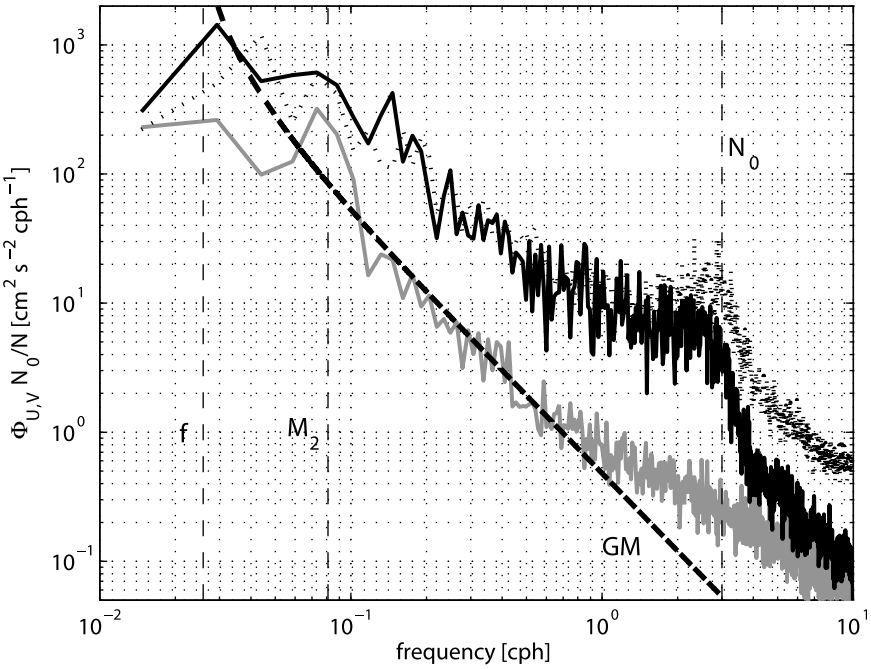

Figure 9. Buoyancy-scaled frequency spectra of horizontal velocity from the continental slope at 265 m depth (1200 kHz ADCP, 205–225 m depth, solid black; 300 kHz ADCP, 125–175 m, dotted black line) and from the Mauritanian shelf close to the coast at 38 m water depth (1200 kHz ADCP, solid gray line). Dashed black line represents the Garret and Munk (GM) frequency spectrum [*Munk*, 1981] for 18°N. Dashed vertical lines mark inertial (f), principle lunar tide (M_2) and buoyancy (N_0 = 3 cph) frequency.

upslope propagating bores for sediment transport in the Faeroe-Shetland Channel. Using sediment traps, they discovered a 100-fold increase in daily sediment flux after the passage of an internal wave packet. Model simulations [*Ribbe and Holloway*, 2001; *Stastna and Lamb*, 2008] along with the body of observations reported in the literature [*Bogucki et al.*, 1997, 2005; *Carter et al.*, 2005; *Hosegood et al.*, 2004] leave little doubt that internal waves in the coastal ocean play a crucial role in sediment resuspension and are able to mix up nutrients into the euphotic zone [*Colosi et al.*, 2001].

4. Fine-Scale Scaling of Turbulent Dissipation

[33] As described in the previous section, velocity and density fluctuations along the Mauritanian continental slope and on the shelf break are often related to nonlinear internal waves and turbulence is elevated compared to other slope and shelf regions. In this section we assess the applicability of fine-scale parameterizations for turbulent dissipation rates using physical properties of background conditions that allow estimates of mixing from more easily observed variables, e.g., for inferring nutrient fluxes or mixing parameterizations in numerical models. Dissipation rates from the microstructure data set are thus compared to fine-scale parameterizations using simultaneously measured fine-scale velocity and CTD data. From numerous turbulence parameterizations for shelf and open ocean environments in literature, two formulations have proven robust against microstructure observations. Both of them, however, have not been validated for oceanic regions that are dominated by highly nonlinear internal waves. For shelf regions, *MacKinnon and Gregg* [2003] proposed a fine-scale scaling (herein MG scaling) using low-frequency and low-baroclinic mode shear (S_{lf}):

$$\varepsilon_{MG} = \varepsilon_0 \left(\frac{N}{N_0}\right)\left(\frac{S_{lf}}{S_0}\right), \tag{3}$$

where reference shear (S_0) and buoyancy (N_0) is 3 cph and $\varepsilon_0 = 6.9 \times 10^{-10}$ W kg^{-1}. It was derived from WKB scaling of an analytical model by *Henyey et al.* [1986] describing the energy flux of internal waves to smaller vertical scales due to wave-wave interaction using ray tracing. The constant ε_0 that combines several unknown constants of the scaling was determined by fitting the derived ε_{MG} to observed dissipation rates from the New England shelf during late summer.

[34] Several recent studies have found good agreement of average dissipation rates calculated from MG-scaled velocity (ADCP) and CTD data and observed dissipation rates from microstructure datasets in other continental shelf regions [e.g., *MacKinnon and Gregg*, 2005; *Palmer et al.*, 2008]. Similarly, average turbulent diffusivities inferred from dissipation rates determined by equation (3) from data collected on the southern New England shelf agreed well with turbulent diffusivities inferred from coastal dye releases [*Ledwell et al.*, 2004]. However, MG scaling failed to reproduce dissipation rates during the presence of internal bores in the New England shelf region [*MacKinnon and Gregg*, 2003].

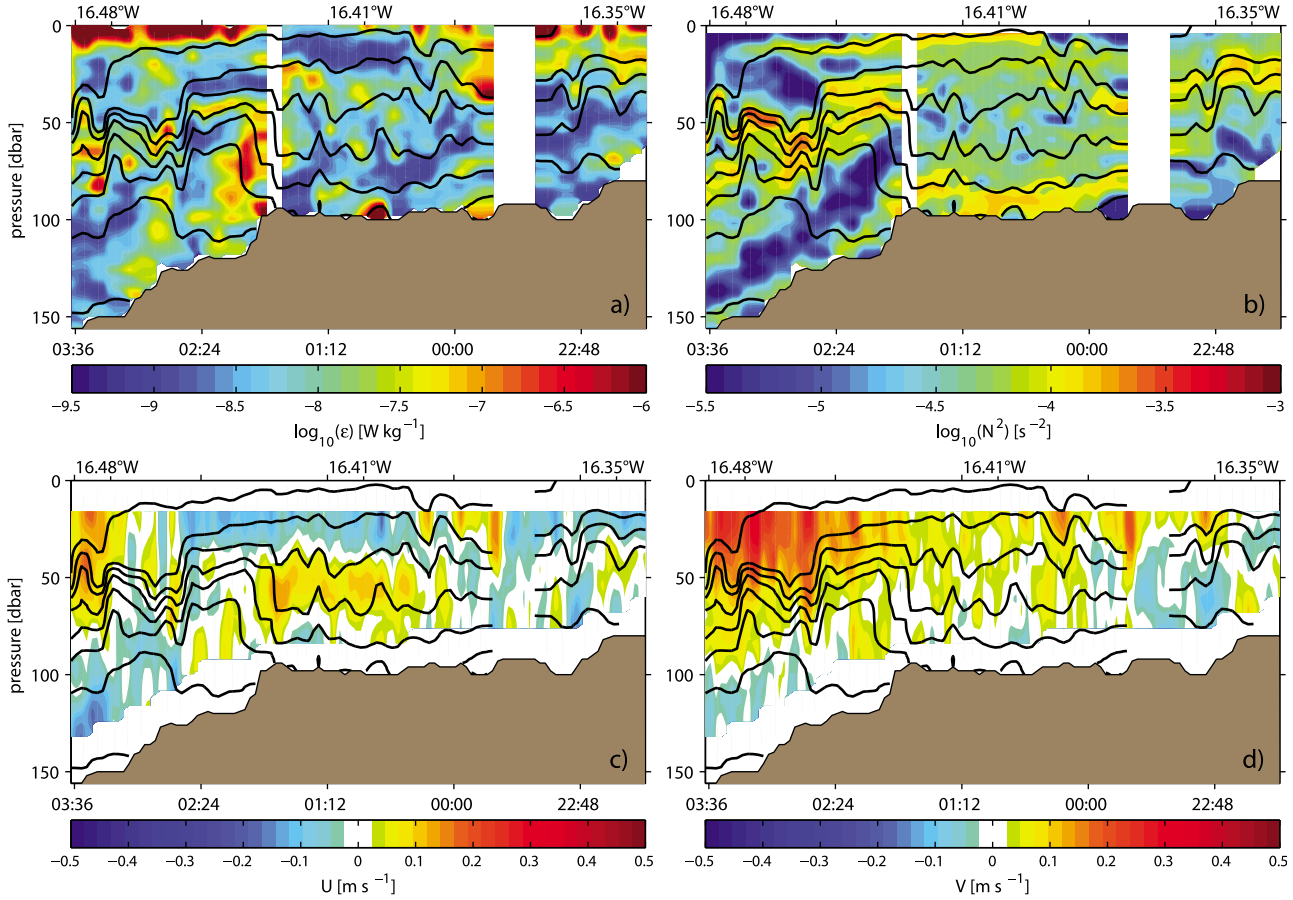

Figure 10. MSS measurements: (a) $\log_{10}$ of turbulent kinetic energy dissipation (ε) and (b) $\log_{10}$ buoyancy frequency squared (N^2). VMADCP measurements: (c) zonal velocity and (d) meridional velocity. On top of each section density distribution is indicated by black contour lines, measured by MSS-Profiler at locations represented by inclined gray dotted lines. In total 45 MSS-profiles used.

[35] Away from oceanic boundaries and background shear flow and in regions where the internal wave field is roughly described by the Garrett-Munk model, wave-wave interaction theory [*Henyey et al.*, 1986] predicts a different scaling. As validated against microstructure data [e.g., *Gregg*, 1989; *Polzin et al.*, 1995; *Gregg et al.*, 2003], average dissipation rates here are related to fine-scale shear and strain as:

$$\varepsilon_1 = \varepsilon_{01} F(R_\omega) L(\theta, N) \left(\frac{N^2}{N_0^2}\right) \left(\frac{S^4}{S_{GM}^4}\right), \qquad (4)$$

where $\varepsilon_{01} = 6.7 \times 10^{-10}$ W kg^{-1}, N_0 = 3 cph, and S_{GM} is the reference shear of the Garrett-Munk spectrum. $F(R_\omega)$ describes the functional dependence of dissipation rate on the frequency content of the internal wavefield [e.g., *Polzin et al.*, 1995] and $L(\theta,N)$ is its dependence on latitude [e.g., *Gregg et al.*, 2003]. Most of the above comparison studies find the scaling to collapse observed average dissipation rates to within a factor of 3.

[36] Restrictions apply for shear (S) calculation as it needs to be determined from internal wave velocity contributions having wave numbers smaller than saturation wave number (i.e., from the near-white part of the shear spectrum) [e.g., *Gargett*, 1990; *Polzin et al.*, 1995]. Additionally, attenuation of shear variance inherent to ADCP velocity measurements needs to be accounted for [*Polzin et al.*, 2002]. Particularly the first issue severely restricts vertical resolution of data comparisons. To avoid this restriction, a simplified scaling is used here. *Gregg* [1989] showed that when the dependency of the internal wave frequency content is omitted and shear is calculated using 10 m binned velocity data, the parameterization still provides some skill in fine-scale scaling of dissipation rates. This often termed Gregg-Henyey scaling (hereinafter GH) is given by

$$\varepsilon_{GH} = 1.8 \times 10^{-6} \left(f \cosh^{-1}\left(\frac{N_0}{f}\right)\right) \left(\frac{N^2}{N_0^2}\right) \left(\frac{S_{10}^4}{S_{GM}^4}\right), \qquad (5)$$

where $L(\theta,N)$ from equation (4) has been substituted with $f \cosh^{-1}(N_0/f)$ and a constant that altered ε_{01}. This formulation further implicitly assumes that the local shear to strain ratio R_ω is 3 (i.e., $F(R_\omega) = 1$).

[37] To compare observed dissipation rates from the continental slope and shelf off Mauritania to MG and GH scaling, we computed the two model dissipation rates ε_{GH} and ε_{MG} in a similar manner as described by *MacKinnon*

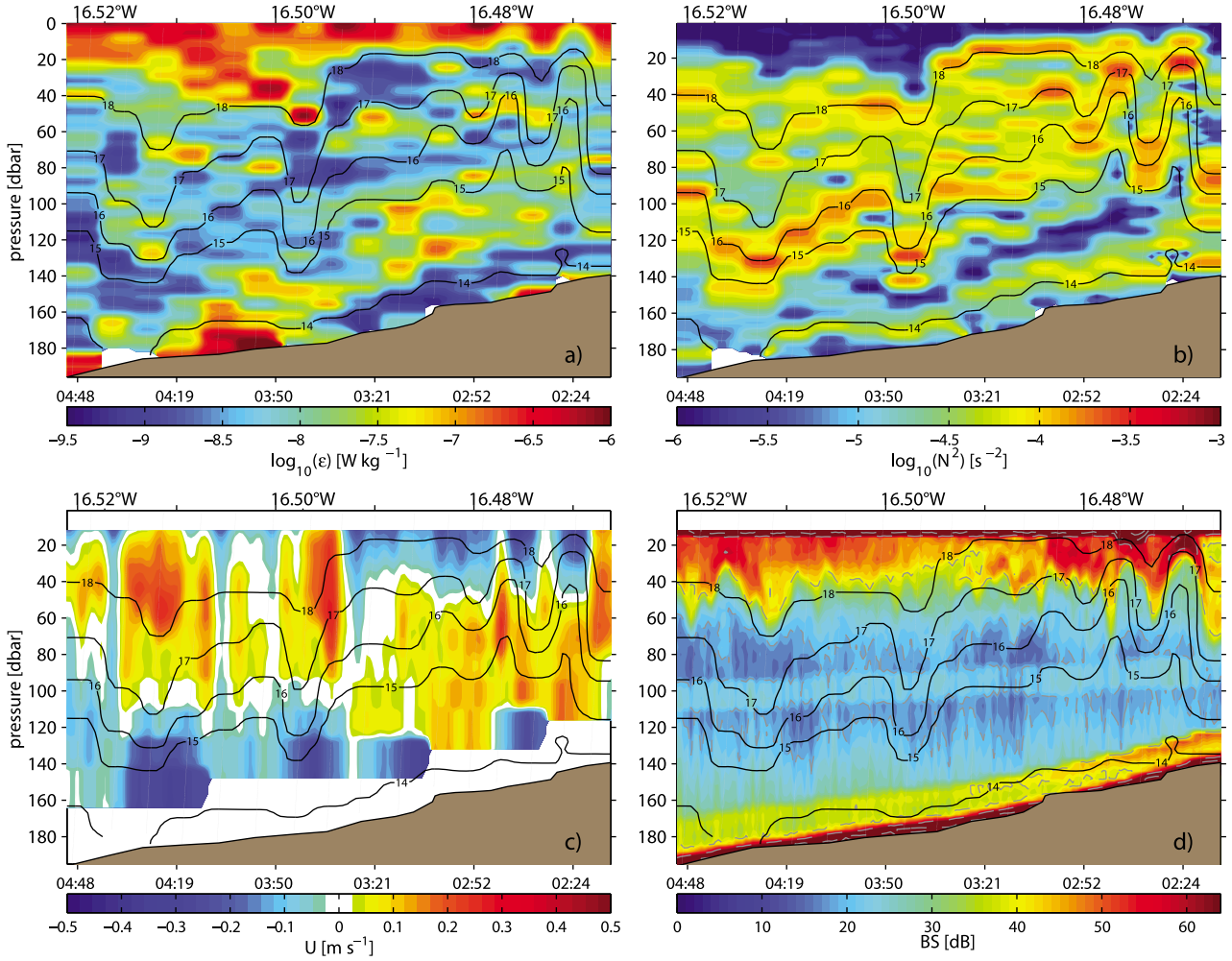

Figure 11. MSS measurements: (a) $\log_{10}$ of turbulent kinetic energy dissipation (ε) and (b) $\log_{10}$ buoyancy frequency squared (N^2). VMADCP measurements: (c) zonal velocity merged and gridded from 300 and 75 kHz ADCP and (d) relative water mass volume backscattering strength (from 300 kHz only). On top of each section temperature distribution is indicated by black contour lines, measured by MSS-Profiler at locations represented by inclined gray dotted lines.

and Gregg [2003]. However, instead of calculating shear from the 8 or 16 m binned ADCP data, shear was calculation from 32 m low-pass filtered 1 h mean ADCP velocity profiles. We found low-pass filtering to be necessary because vertical wave number (k) spectra of velocity shear did not show a k^{-1} dependence for wave numbers larger than the saturation wave number k_c, which is probably due to noise. To account for the loss of shear variance due to low-pass filtering, the scaling variables S_0 in equation (3) and S_{GM} in equation (5) were altered to reflect the reduced wave number range of the shear data. Integrating the Garret and Munk shear spectrum [*Munk*, 1981] to wave numbers smaller than 32^{-1} m^{-1} yields 1.3 cph. Thus, instead of using S_0 = 3 cph in equation (3), which results from the full integration of the GM shear spectrum, S_0 = 1.3 cph was used. Similarly, for S_{GM} in equation (5) 1.3 × (N/N_0) cph (S^4_{GM} = 2.4 ×10^{-11} (N^2/N^2_0)^2) was used. Additionally, lost shear variance due to inherent smoothing of ADCP shear was accounted for all wave numbers smaller than 32^{-1} m^{-1} using sinc^4(Δx k), where Δx is the bin length of ADCP data and sinc(x) = sin(πx)/(πx), following *Polzin et al.* [2002]. It should be noted that correction for attenuation of ADCP shear for the wavelength interval used here is small and accounts for less than 10% of the observed shear variance. The results shown in the following paragraphs should thus remain comparable to previous studies that did not account for shear attenuation by ADCPs.

[38] Following *MacKinnon and Gregg* [2003], observed dissipation rates and N^2 data were vertically smoothed using a 16 m Bartlett window and subsampled on 8 m depth bins to match the ADCP sampling. Because of the deficiencies of the ADCP velocity measurements in the near-surface and bottom layers, comparisons from those depth intervals are excluded (VMADCPs are not able to provide reliable velocity measurements in the lower 15% of the water column because of sidelobe interferences). Regions in the water column, where Richardson numbers dropped below 0.25 (about 4% of the available 8 m estimates), are excluded as both parameterizations do not apply when Kelvin-Helmholtz instabilities occur. Because of these constraints, most of the data from bands of low stratification discussed in the previous section are excluded. All available observations

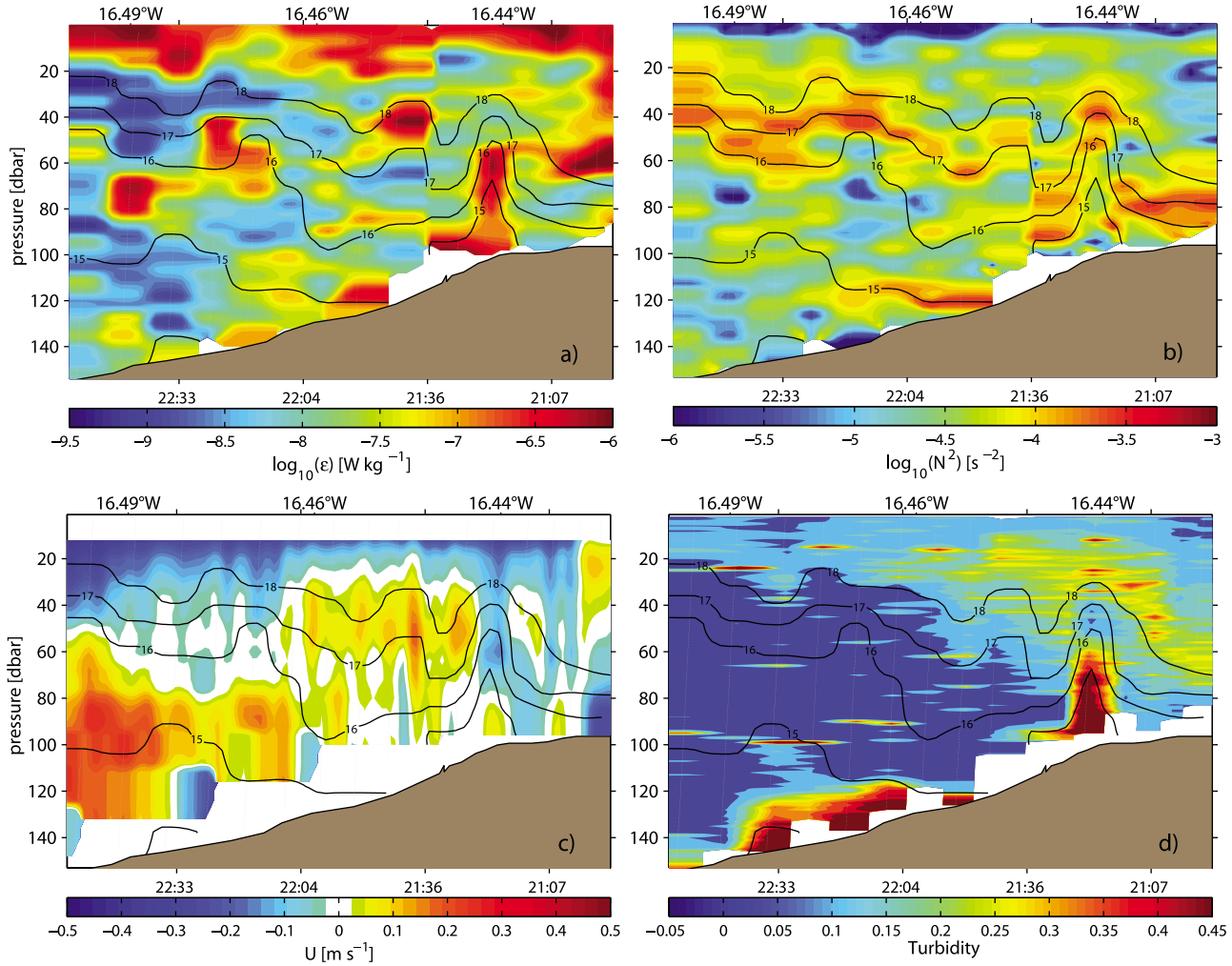

Figure 12. Same as Figure 11 except for (d) where optical turbidity observed by MSS-profiler is shown.

from shoreward of the 450 m isobaths are used in the comparison. This data set comprises 250 microstructure, CTD, and 1 h ADCP profiles from the continental slope and 210 profiles microstructure, CTD, and ADCP profiles from the shelf region resulting in 2900 and 900 individual 8 m binned estimates of ε_{GH} and ε_{MG}, respectively.

[39] As noted in section 3, mean observed dissipation rates from waters shallower than 450 m were elevated and yielded $\varepsilon_{obs} = 4.9 \times 10^{-8}$ W kg^{-1}. Mean dissipation rate calculated from GH scaling (ε_{GH}) was somewhat lower and yielded 1.7×10^{-8} W kg^{-1}. Considering that the average frequency content at the continental slope compared to GM is shifted toward gravity wave frequency (Figure 9), the GH average ε_{GH} compares quite well to ε_{obs}. In fact, shear to strain ratios ($R\omega$) determined from ADCP and CTD data yielded values between 1.5 and 2. This would imply $F(R_\omega)$ in equation (4) to be larger than a factor of 2 [e.g., *Kunze et al.*, 2006]. Thus, average dissipation rate from wave-wave interaction parameterization in equation (4) should be within a factor of 2 of the observations. The variability of ε_{GH} was also quite similar to the variability of ε_{obs} ($1.0 \times 10^{-12} \leq \varepsilon_{GH} \leq 1.5 \times 10^{-6}$ W kg^{-1} versus $3.1 \times 10^{-10} \leq \varepsilon_{obs} \leq 2.5 \times 10^{-6}$ W kg^{-1}), when considering the noise level of the instruments. However, individual estimates of ε_{GH} and ε_{obs} show large scatter (black dots in Figure 13c), indicating that a one-to-one relationship between observed and model dissipation is absent.

[40] Average dissipation rate from the MG scaling (ε_{MG}) was more than a factor of 20 lower than ε_{obs}. In order to agree with the observed average, the constant ε_0 in equation (3) had to be altered to $\varepsilon_0 = 1.6 \times 10^{-8}$ W kg^{-1}. Separately determined ε_0 for slope and shelf region were within a factor of two with a lower value for the shelf. The scatter of individual ε_{MG} estimates ($9.1 \times 10^{-10} \leq \varepsilon_{MG} \leq 8.7 \times 10^{-7}$ W kg^{-1}) was less widespread than the scatter of the observations. Similarly to the GH scaling, individual ε_{MG} and ε_{obs} determined from simultaneous measurements show no clear relationship (Figure 13f, black dots). The fact that ε_0 is ad hoc unknown makes the MG scaling of limited applicability. Similar to the results above, previous studies have shown that ε_0 varies for different season at the same location (i.e., for variable N in the depth range of the seasonal thermocline) [*MacKinnon and Gregg*, 2005] and for different shelf regions [e.g., *Carter et al.*, 2005; *Palmer et al.*, 2008]. The value for ε_0 determined here is the highest value compared to previous studies. Similarly, our average dissipation rates

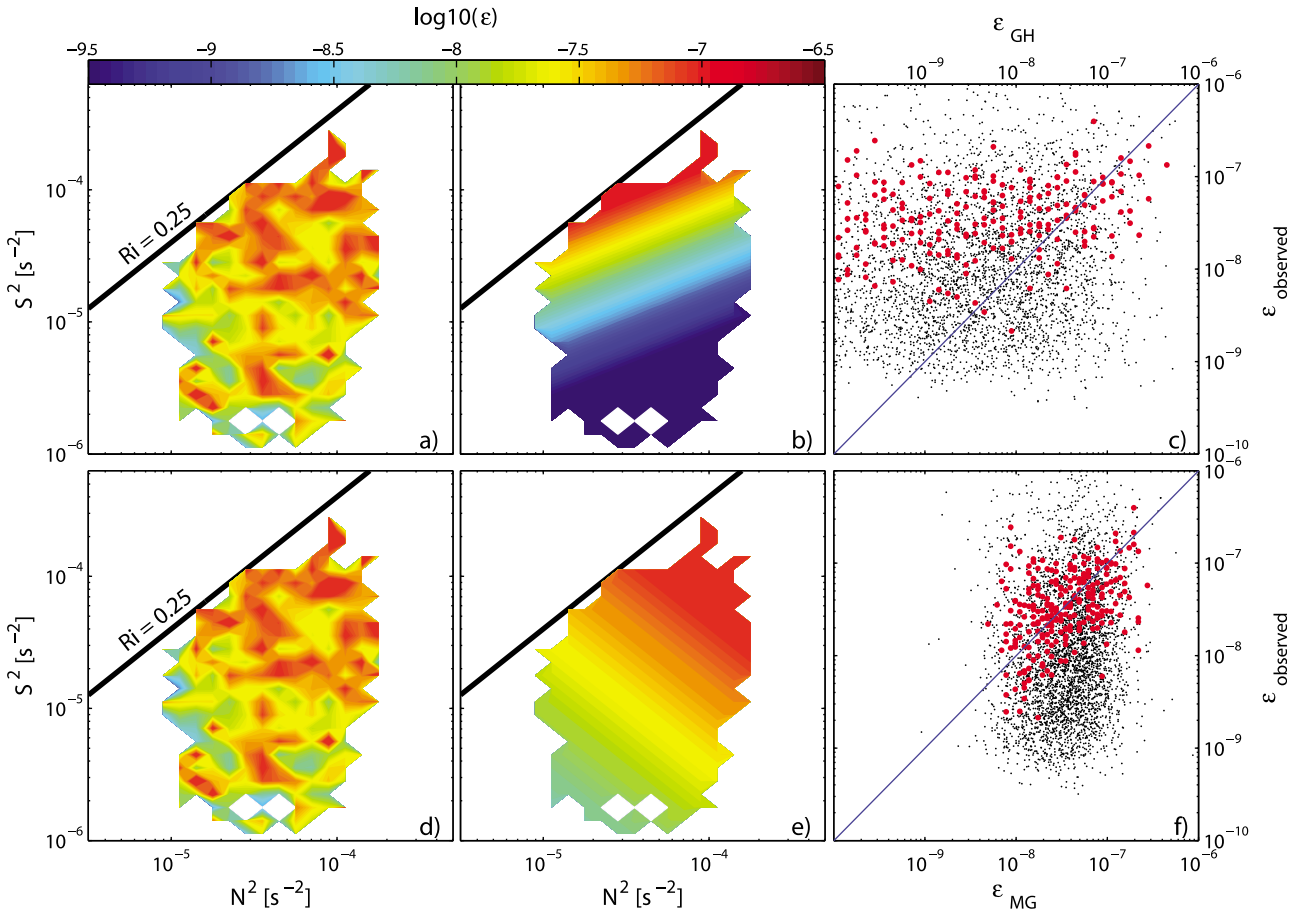

Figure 13. (a, d) Averaged observed dissipation data binned in logarithmically spaced bins of stratification and shear variance. Only data with Ri > 1/4 are shown. For comparison, the functional dependence of the GH and MG parameterization on (b) shear variance and (e) stratification is shown. (c, f) Individual (black) and bin-averaged (red) parameterized dissipation rates ε_{GH} and ε_{MG} against the observations, ε_{obs}.

on the continental slope are larger than those reported in the other studies that found lower ε_0. *Carter et al.* [2005] suggested that some underlying physics in the MG scaling, like wave scattering from topography and energy transfer to higher wave numbers, might be unaccounted for.

[41] Despite the shortcomings of the MG scaling for this data, previous studies have shown that the functional dependence of ε_{obs} on shear and stratification is better represented by the MG scaling than by GH scaling [e.g., *Carter et al.*, 2005; *Palmer et al.*, 2008]. The functional dependence of the dissipation rates is best illustrated when ε_{obs} are averaged in logarithmic bins of S^2 and N^2 (Figures 13a and 13d). In this respect, the major difference between the two parameterizations is that for fixed shear dissipation rates decrease with increasing stratification for GH scaling (Figure 13b) while they increase for MG scaling (Figure 13e). When comparing the observed S^2 and N^2 binned dissipation rates to the distribution predicted by the two parameterizations there is no clear agreement with either of the two. However, there is some indication that bin average dissipation rates increases for increasing stratification, in particular for buoyancy values of $N^2 \sim 10^{-4}$ s^{-2} and relatively low shear ($S^2 < 5 \times 10^{-5}$ s^{-2}; Figures 13a and 13c, red dots) but this relationship is weak.

[42] The results here were obtained from a continental slope that is frequently near-critical or critical for the M_2 frequency. A near-critical slope favors the development of nonlinear internal waves that were presented in the previous sections. In turn, it is suggested that these nonlinear waves are dominantly responsible for the elevated dissipation rates that were observed in this region. As shear contributions from those waves are strongly damped in the 1 h mean low-mode velocity profiles that are used in the shear calculation for the two parameterizations, the degree of nonlinearity of the internal waves remains unaccounted for. This probably explains the lack of a clear functional dependence of ε_{obs} for shear and buoyancy variance that has been found for previous studies in regions where linear internal wave were dominant. A rather unexpected result is the good agreement between the observed average dissipation rate and the average dissipation rate determined from wave-wave interaction parameterization in equation (4). Internal wave-wave interaction theory [*Henyey et al.*, 1986] did not consider the development of nonlinear internal waves that are frequently observed off Mauritania nor was internal wave interaction with topography accounted for in their model. Nevertheless, *Carter et al.* [2005] similarly found good agreement

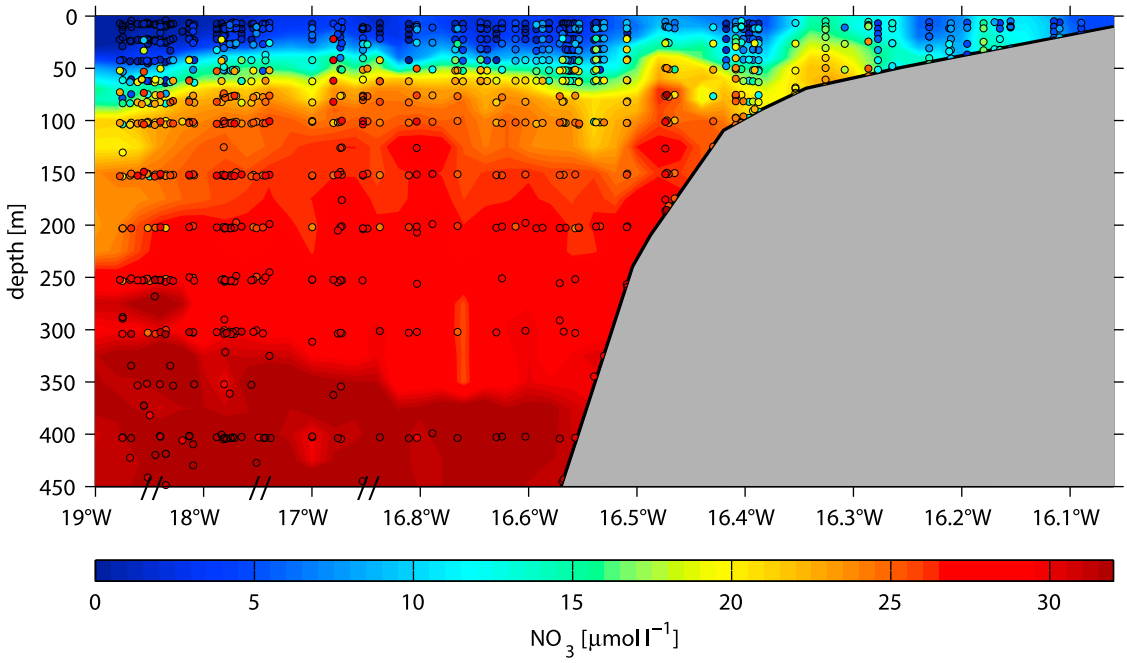

Figure 14. Composite zonal section of nitrate distribution compiled from all water samples collected during high upwelling. Individual samples are indicated by colored dots.

between average dissipation rates form observations and those determined from equation (4) in a data set from the Monterey Bay shelf.

5. Nutrient Fluxes

[43] Coastal upwelling areas constitute regions of strong biological production due to the nutrient supply to the surface from deeper levels. In the absence of turbulence and instantaneous consumption, upwelling represents a reversible transport of fluid back and forth across the shelf. Turbulent mixing is the irreversible part of the process that acts to replenish the store of nutrients on the shelf and to mix it up higher within the water column so that it becomes available for photosynthesis. Here, we quantify the flux of nitrate due to turbulence to assess the importance of diapycnal nutrient fluxes in the Mauritanian upwelling region.

[44] The vertical flux of nitrate by turbulent mixing was calculated by multiplying the eddy diffusivity with the vertical nitrate concentration gradients, $Flux_{NO3} = K_\rho dNO_3/dz$. A detailed description of the calculation is given in Appendix A. The choice of the depth interval for calculation of diapycnal nitrate fluxes relevant for photosynthesis is somewhat arbitrary. Some studies [e.g., *Hales et al.*, 2005] use a depth interval where largest nitrate gradients occur while others use the flux across the base of the mixed layer. A composite of all nitrate data projected (according to water depth) on a zonal section shows that these zones are partly collocated (Figure 14). Strongest vertical gradients of nitrate concentrations occur mostly slightly below the mixed layer, in depth of about 40–60 m (ascending toward the coast). From chlorophyll sampling within the upwelling region it was indicated that phytoplankton preferentially accumulates at the base of the mixed layer. Thus, here the diapycnal flux of nitrate just below the mixed layer is determined as it appears to be most relevant for biological production in the upwelling region.

[45] The distribution of nitrate concentration further reveals that in offshore regions surface waters are mostly nitrate depleted, whereas above the continental slope and shelf near-surface nitrate concentrations occasionally exceed 5 μmol L^{-1} were observed (Figure 14). A regional subdivided histogram (Figure 15) of all available nitrate flux estimates (in total 95) from the three cruises during high upwelling season shows that averaged fluxes differ considerably between the different topographic environments. Averaged fluxes are 1.2 (0.6–1.7) $\times 10^{-2}$ μmol m^{-2} s^{-1} for offshore stations, 11.8 (4.9–20.7) $\times 10^{-2}$ μmol m^{-2} s^{-1} for stations above the slope, and 4.3 (0.2–11.2) $\times 10^{-2}$ μmol m^{-2} s^{-1} for the shelf region (values in brackets denote lower and upper statistical uncertainty limits, see Appendix A). On average, values above the continental slope exceed open ocean values by a factor of 10. On the shelf, lower fluxes compared to the continental slope are predominately due to prevailing weak vertical gradients of nitrate concentration. The large scatter of individual flux estimates (over more than 3 decades, Figure 15) suggests that fluxes are dominated by sporadic mixing events.

[46] Previous estimates of turbulent nitrate fluxes in other shallow water regions are of lower (about 1–4 $\times 10^{-2}$ μmol m^{-2} s^{-1} [e.g., *Sharples et al.*, 2001a, 2007; *Hales et al.*, 2009; *Rippeth et al.*, 2009]) or of similar magnitude (6–14 $\times 10^{-2}$ μmol m^{-2} s^{-1}, [e.g., *Sharples et al.*, 2001b; *Hales et al.*, 2005, 2009]). Most of these studies generally suggest that a significant part of total biological production on the shelves and continental slopes is driven by these turbulent nutrient fluxes. Although our nitrate flux estimates are at the upper end of previously presented fluxes, a direct

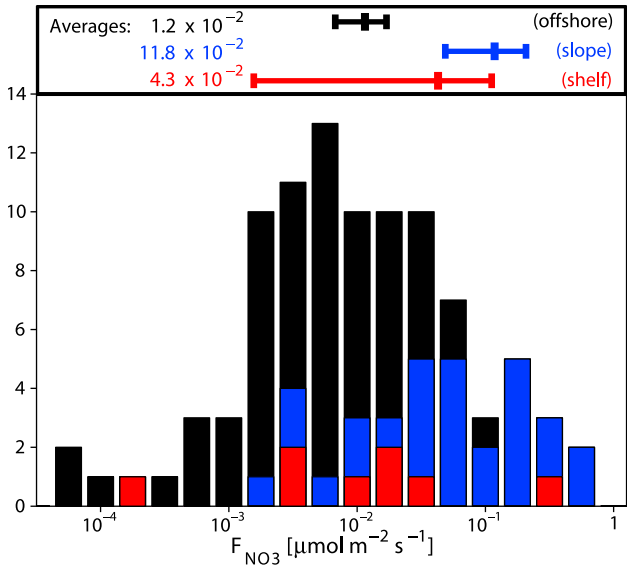

Figure 15. Logarithmic-spaced histogram of nitrate fluxes at the base of the mixed layer in different regional settings (color): on the shelf (water depth <95 m, red), above the continental slope (depth between 95 and 450 m, blue), and offshore (depth >450 m, black). Upper panel indicates regional averages and their statistical uncertainty.

biological impact in the upwelling environment off Mauritanian is not obvious.

[47] To evaluate the importance of turbulent transport of nitrate for the biological demand, the observed fluxes were used to estimate the biological production rate that can by maintained by the fluxes. Assuming validity of the Redfield ratio (C:N ~6.6) for phytoplankton, an averaged flux of 12×10^{-2} μmol m^{-2} s^{-1} would support a potential carbon fixation rate of 0.8 g C m^{-2} d^{-1}. The biological parameter to which this value should directly compare is net community production (NCP) [e.g., *Hales et al.*, 2005]. *Minas et al.* [1986] estimated a NCP of 2.3 g C m^{-2} d^{-1} during maximum upwelling for an approximately 60 km wide strip along the coast north of our study region. A similar production rate, 1.4 ± 0.4 g C m^{-2} d^{-1} for a 200 km wide region, were obtained recently for the Mauritanian upwelling region for February from measured CO_2 and N_2O concentrations in surface waters (T. Steinhoff, personal communication, 2009). Both estimates exceed the potential carbon fixation rate supported by diapycnal nitrate fluxes presented in Figure 15. When taking into account the varying offshore extensions of the reported NCP estimates, diapycnal nitrate fluxes seem to play only a minor role for the nutrients balance in the upwelling region by contributing 10–25% to the NCP.

6. Summary and Conclusions

[48] The inclination of the seafloor in the upper 600 m of the Mauritanian continental slope is dominantly near critical for the baroclinic M_2 tide during winter stratification. This setting supports the generation of internal tides, bores, and nonlinear internal wave trains. Velocity observations from VMADCPs from three cruises and velocity time series from short-term mooring deployments from the continental slope and shelf region off Mauritanian collected during the maximum upwelling season exhibits characteristics of all of these features.

[49] Most prominent in the velocity data from the continental slope were bores with maximum horizontal velocity signals at middepth. These bores have horizontal and vertical scales of 2–3 km and 50–100 m, respectively. Associated strong pulse-like onshore and southward velocity signals frequently exceed 0.3–0.4 m s^{-1}. The occurrence of the bores is irregular with respect to the tidal cycle, but in general two bores were observed during a 24 h period. The velocity structures of the observed bores are in general agreement with numerical simulations of bores developing on the continental slope [*Vlasenko and Hutter*, 2002; *Legg and Adcroft*, 2003]. Because of the presence of the bores and associated nonlinear internal wave trains at the continental slope, buoyancy-scaled spectra of horizontal velocity are strongly elevated by 1–2 decades compared to GM scaling at higher frequency, whereas shelf spectra do not show elevated energy levels at these time scales.

[50] *Legg and Adcroft* [2003] demonstrated that upslope-propagating bores in model simulations appear over a range of slopes, regardless of the specific shape of the seafloor, as long as the Froude number of the reflected wave exceeds 1. They determined a range of topographic angles $\theta_1 < \theta < \theta_2$ for which bores are generated, defined by:

$$\tan(\theta_1) = s\frac{Fr_I^{-1/2} - 1}{Fr_I^{-1/2} + 1} \quad \text{and} \quad \tan(\theta_2) = s\frac{Fr_I^{-1/2} + 1}{Fr_I^{-1/2} - 1},$$

where $Fr_I = (U_0)_I/(cp)_I$ is the Froude number of the incoming wave. With increasing stratification the internal wave characteristic, s, would be reduced, as would the Froude number for a wave with given amplitude. Hence the range of angles over which bore formation might occur would be limited. Under this concept, it is anticipated that low stratification due to upwelling may be key to the elevated energy of bores and nonlinear internal waves that were observed on the continental slope. During summer, the lack of upwelling favorable conditions enhances stratification along the continental slope and thus may reduce the development of bores and associated mixing off Mauritania.

[51] Microstructure observations reveal that the continental slope off Mauritanian is a mixing hot spot. Average turbulent dissipation rate is 4.9×10^{-8} W kg^{-1} and peaks near the shelf break. Here, integrated dissipation peaks at 30 mW m^{-2} and the mean value for the approximately 20 km wide strip between the 450 and 95 m isobaths yielded 13 mW m^{-2}. Yo-yo microstructure profiling transects support the idea of frequently existing patches of intense mixing within the seasonal thermocline that are caused by elevated shear due to nonlinear internal waves. The broad maximum close to N in the frequency spectrum of horizontal velocity at the continental slope indicates the availability of enhanced kinetic energy on small temporal and spatial scales. A recurring feature to the presented transects are bands of low stratification partly collocated with high dissipation rates. Acoustic backscatter images as well as turbidity observations conducted suggest that sediment resuspends because of the

presence of near-bottom intensified waves close to the shelf break. Cross-shelf transects show high ε and high turbidity at sharp near-bottom fronts.

[52] A comparison of fine-scale internal wave-wave interaction parameterization of turbulent dissipation rates [e.g., *Gregg*, 1989; *Polzin et al.*, 1995; *Gregg et al.*, 2003], as well as a more recently developed fine-scale parameterization for shelf regions [*MacKinnon and Gregg*, 2003] to the microstructure measurements showed deficiencies in reproducing the dissipation rates from the Mauritanian continental slope and shelf. The major difference to studies from other slope and shelf regions that found agreement between observed and parameterized dissipation rates is the frequent occurrence of nonlinear internal waves at the continental slope off Mauritania. Shear and buoyancy contributions from those waves are not well represented in fine-scale data (typically 1 h averaged and 16 m vertically smoothed velocities), while they contribute substantially to turbulence. Because the slope and shelf regions of the ocean, in which nonlinear internal waves are predominate, appear to be an important contributor to tidal dissipation and diapycnal fluxes, it is concluded that a general parameterization of mixing for continental slopes and shelf regions does not exist. In fact, the lack of a clear functional dependence of ε_{obs} to fine-scale shear and buoyancy in our data set indicates a more general parameterization, if at all possible, would require shear to be resolved at higher vertical and temporal scale.

[53] Finally, although diapycnal nutrient fluxes at the continental slope are amongst the largest published to date, their overall contribution to net community production in the large-scale Mauritanian upwelling region is only in the order of 10% to 25%. This indicates that other nutrient supply pathways (e.g., vertical advection/lateral eddy fluxes) have to be considered for the nutrient balance in this heavily productive upwelling region.

Appendix A

A1. NO_3 Flux Calculation

[54] Nitrate concentration data were available from CTD bottle samples that were collected immediately prior or after microstructure profiling. Typical vertical spacing of the nitrate data was 10 m in the top 40 m of the water column and 20 m below (Figure 14). The mixed layer depth (MLD) was defined as the depth where potential density is increased by 0.125 kg m^{-3} compared to a reference value at 6 m depth. Flux calculations ($F_{NO3} = K_\rho dNO_3/dz$) were then performed for the depth interval from 5 m below the MLD to 15–25 m below the MLD. The variable lower boundary was dependent on availability of nitrate concentration measurements from the bottle data needed for nitrate concentration gradient calculations. Eddy diffusivities for the flux calculation were determined by arithmetically averaging K_ρ from all available microstructure casts performed on each station (usually 3–5, see section 2) within the selected depth interval.

A2. Standard Error of NO_3 Fluxes

[55] To evaluate uncertainties of averaged fluxes we used Gaussian error propagation to determine the standard error of average diapycnal diffusivity:

$$\Delta K_\rho = K_\rho \left[\left(\frac{\Delta \Gamma}{\Gamma} \right)^2 + \left(\frac{\Delta \varepsilon}{\varepsilon} \right)^2 + \left(\frac{\Delta N^2}{N^2} \right)^2 \right]^{1/2}$$

where Δ denote the absolute uncertainty of the various average variables. This procedure is similar to estimates of uncertainties in the variance budgets of buoyancy recently published by *Ferrari and Polzin* [2005]. For $\Delta\Gamma$, a constant value of 0.04 is used as suggested by *St. Laurent and Schmitt* [1999]. The absolute uncertainty ΔN^2 was determined by the standard error of the depth averaged N^2 from individual stations for each of the three topographic environments. The standard error here refers to the standard deviation divided by the square root of the number of estimates. Finally, the statistical uncertainty of ε is calculated using a bootstrap method [*Efron*, 1979].

[56] Accordingly, the uncertainty on the estimates of averaged turbulent nitrate fluxes is given by:

$$\Delta Flux_{NO3} = Flux_{NO3} \left[\left(\frac{\Delta K_\rho}{K_\rho} \right)^2 + \left(\frac{\Delta \partial_z [NO_3]}{\partial_z [NO_3]} \right)^2 \right]^{1/2}$$

where $\Delta\partial_z [NO_3]$ denotes the standard error of mean vertical gradients of nitrate concentrations. It should be noted that the analysis does not include biases or uncertainties due to measurement error. The error of the flux calculation may thus be larger than the statistical presented.

[57] **Acknowledgments.** Financial support for this study was provided by the Deutsche Forschungsgemeinschaft as part of the Emmy Noether Program (DE1369/1-1) and as part of the MUMP (grant DE1369/3-1). We would like to thank Captain Schneider and his crew of R/V Poseidon for professional support during cruise P347. Cruises P348 and M68/3 were part of the joint project SOPRAN funded by Bundesministerium für Bildung und Forschung grant 03F0462A. We thank the authorities of Mauritania for the permission to work in their territorial waters. We are indebted to Rebecca Hummels who helped with data processing.

References

Apel, J. R. (2003), A new analytical model for internal solitons in the ocean, *J. Phys. Oceanogr.*, *33*, 2247–2269.

Baines, P. G. (1982), On internal tide generation models, *Deep Sea Res.*, *29*(3), 307–338.

Barton, E. D., J. Arístegui, P. Tett, M. Cantón, J. García-Braun, S. Hernández-León, L. Nykjaer, C. Almeida, J. Almunia, S. Ballesteros, et al. (1998), The transition zone of the Canary Current upwelling region, *Prog. Oceanogr.*, *41*(4), 455–504.

Bogucki, D., T. Dickey, and L. G. Redekopp (1997), Sediment resuspension and mixing by resonantly generated internal solitary waves, *J. Phys. Oceanogr.*, *27*(7), 1181–1196.

Bogucki, D. J., L. G. Redekopp, and J. Barth (2005), Internal solitary waves in the Coastal Mixing and Optics 1996 experiment: Multimodal structure and resuspension, *J. Geophys. Res.*, *110*, C02024, doi:10.1029/2003JC002253.

Carter, G. S., M. C. Gregg, and R. C. Lien (2005), Internal waves, solitary-like waves, and mixing on the Monterey Bay shelf, *Cont. Shelf Res.*, *25*(12–13), 1499–1520.

Colosi, J. A., R. C. Beardsley, J. F. Lynch, G. Gawarkiewicz, C. S. Chiu, and A. Scotti (2001), Observations of nonlinear internal waves on the outer New England continental shelf during the summer Shelfbreak Primer study, *J. Geophys. Res.*, *106*(C5), 9587–9601, doi:10.1029/2000JC900124.

Duda, T. F., et al. (2004), Internal tide and nonlinear internal wave behavior at the continental slope in the northern South China Sea, *IEEE J. Oceanic Eng.*, *29*(4), 1105–1130.

Efron, B. (1979), 1977 Rietz Lecture—Bootstrap methods—another look at the jackknife, *Ann. Stat.*, *7*, 1–26.

Eriksen, C. C. (1982), Observations of internal wave reflection off sloping bottoms, *J. Geophys. Res.*, *87*(C1), 525–538, doi:10.1029/JC087iC01p00525.

Eriksen, C. C. (1985), Implications of ocean bottom reflection for internal wave spectra and mixing, *J. Phys. Oceanogr.*, *15*(9), 1145–1156.

Eriksen, C. C. (1998), Internal wave reflection and mixing at Fieberling Guyot, *J. Geophys. Res.*, *103*(C2), 2977–2994, doi:10.1029/97JC03205.

Ferrari, R., and K. L. Polzin (2005), Finescale structure of the T-S relation in the eastern North Atlantic, *J. Phys. Oceanogr.*, *35*(8), 1437–1454.

Fischer, J., P. Brandt, M. Dengler, M. Müller, and D. Symonds (2003), Surveying the upper ocean with the Ocean Surveyor: a new phased array Doppler current profiler, *J. Atmos. Oceanic Technol.*, *20*, 742–751.

Gargett, A. E. (1990), Do We Really Know How to Scale the Turbulent Kinetic Energy Dissipation Rate ε Due to Breaking of Oceanic Internal Waves?, *J. Geophys. Res.*, *95*(C9), 15,971–15,974, doi:10.1029/JC095iC09p15971.

Gerkema, T., and J. T. F. Zimmerman (1995), Generation of nonlinear internal tides and solitary waves, *J. Phys. Oceanogr.*, *25*(6), 1081–1094.

Gnanadesikan, A., R. D. Slater, N. Gruber, and J. L. Sarmiento (2002), Ocean vertical exchange and new production: A comparison between models and observations, *Deep Sea Res.*, *49*, 363–401.

Gregg, M. C. (1989), Scaling turbulent dissipation in the thermocline, *J. Geophys. Res.*, *94*(C7), 9686–9698, doi:10.1029/JC094iC07p09686.

Gregg, M. C. (1999), Uncertainties and limitations in measuring ε and χ_T, *J. Atmos. Oceanic Technol.*, *16*(11), 1483–1490.

Gregg, M. C., T. B. Sanford, and D. P. Winkel (2003), Reduced mixing from the breaking of internal waves in equatorial waters, *Nature*, *422*, 513–515.

Hales, B., N. Moum, P. Covert, and A. Perlin (2005), Irreversible nitrate fluxes due to turbulent mixing in a coastal upwelling system, *J. Geophys. Res.*, *110*, C10S11, doi:10.1029/2004JC002685.

Hales, B., D. Hebert, and J. Marra (2009), Turbulent supply of nutrients to phytoplankton at the New England shelf break front, *J. Geophys. Res.*, *114*, C05010, doi:10.1029/2008JC005011.

Henyey, F. S., J. Wright, and S. M. Flatte (1986), Energy and action flow through the internal wave field—An eikonal approach, *J. Geophys. Res.*, *91*(C7), 8487–8495, doi:10.1029/JC091iC07p08487.

Holloway, P. E. (1985), A comparison of semidiurnal internal tides from different bathymetric locations on the Australian north-west shelf, *J. Phys. Oceanogr.*, *15*(3), 240–251.

Holloway, P. E., and M. A. Merrifield (1999), Internal tide generation by seamounts, ridges, and islands, *J. Geophys. Res.*, *104*(C11), 25,937–25,951, doi:10.1029/1999JC900207.

Hosegood, P., J. Bonnin, and H. van Haren (2004), Solibore-induced sediment resuspension in the Faeroe-Shetland Channel, *Geophys. Res. Lett.*, *31*, L09301, doi:10.1029/2004GL019544.

Inall, M. E., T. P. Rippeth, and T. J. Sherwin (2000), Impact of nonlinear waves on the dissipation of internal tidal energy at a shelf break, *J. Geophys. Res.*, *105*(C4), 8687–8705, doi:10.1029/1999JC900299.

Klymak, J. M., and J. N. Moum (2003), Internal solitary waves of elevation advancing on a shoaling shelf, *Geophys. Res. Lett.*, *30*(20), 2045, doi:10.1029/2003GL017706.

Kunze, E., E. Firing, J. M. Hummon, T. K. Chereskin, and A. M. Thurnherr (2006), Global abyssal mixing inferred from lowered ADCP shear and CTD strain profiles, *J. Phys. Oceanogr.*, *36*(8), 1553–1576.

Ledwell, J. R., T. F. Duda, M. A. Sundermeyer, and H. E. Seim (2004), Mixing in a coastal environment: 1. A view from dye dispersion, *J. Geophys. Res.*, *109*, C10013, doi:10.1029/2003JC002194

Legg, S., and A. Adcroft (2003), Internal wave breaking at concave and convex continental slopes, *J. Phys. Oceanogr.*, *33*(11), 2224–2246.

Lueck, R. G., F. Wolk, and H. Yamazaki (2002), Oceanic velocity microstructure measurements in the 20th century, *J. Oceanogr.*, *58*(1), 153–174.

MacKinnon, J. A., and M. C. Gregg (2003), Mixing on the late-summer New England shelf - Solibores, shear, and stratification, *J. Phys. Oceanogr.*, *33*(7), 1476–1492.

MacKinnon, J. A., and M. C. Gregg (2005), Spring mixing: Turbulence and internal waves during restratification on the New England shelf, *J. Phys. Oceanogr.*, *35*(12), 2425–2443.

Minas, H. J., M. Minas, and T. T. Packard (1986), Productivity in upwelling areas deduced from hydrographic and chemical fields, *Limnol. Oceanogr.*, *31*, 1182–1206.

Moum, J. N., and J. D. Nash (2000), Topographically induced drag and mixing at a small bank on the continental shelf, *J. Phys. Oceanogr.*, *30*(8), 2049–2054.

Moum, J. N., M. C. Gregg, R. C. Lien, and M. E. Carr (1995), Comparison of turbulent kinetic-energy dissipation rate estimates from 2 ocean microstructure profilers, *J. Atmos. Oceanic Technol.*, *12*(2), 346–366.

Moum, J. N., D. M. Farmer, W. D. Smyth, L. Armi, and S. Vagle (2003), Structure and generation of turbulence at interfaces strained by internal solitary waves propagating shoreward over the continental shelf, *J. Phys. Oceanogr.*, *33*(10), 2093–2112.

Munk, W. (1981), Internal waves and small-scale processes, in *Evolution of Physical Oceanography*, edited by B. A. Warren and W. Carl, pp. 264–290, MIT Press, Cambridge, U. K.

Nasmyth, P. W. (1970), Oceanic turbulence, Ph.D. thesis, 69 pp., Inst. Oceanogr., Univ. British Columbia, Vancouver, Canada.

Oakey, N. S. (1982), Determination of the rate of dissipation of turbulent energy from simultaneous temperature and velocity shear microstructure measurements, *J. Phys. Oceanogr.*, *12*(3), 256–271.

Osborn, T. R. (1974), Vertical profiling of velocity microstructure, *J. Phys. Oceanogr.*, *4*(1), 109–115.

Osborn, T. R. (1980), Estimates of the local-rate of vertical diffusion from dissipation measurements, *J. Phys. Oceanogr.*, *10*(1), 83–89.

Palmer, M. R., T. P. Rippeth, and J. H. Simpson (2008), An investigation of internal mixing in a seasonally stratified shelf sea, *J. Geophys. Res.*, *113*, C12005, doi:10.1029/2007JC004531.

Phillips, O. M. (1977), *The Dynamics of the Upper Ocean*, 2nd ed., 336 pp., Cambridge Univ. Press, New York.

Pingree, R. D., G. T. Mardell, and A. L. New (1986), Propagation of internal tides from the upper slopes of the Bay of Biscay, *Nature*, *321*(6066), 154–158.

Polzin, K. L., J. M. Toole, and R. W. Schmitt (1995), Finescale parameterizations of turbulent dissipation, *J. Phys. Oceanogr.*, *25*(3), 306–328.

Polzin, K., E. Kunze, J. Hummon, and E. Firing (2002), The finescale response of lowered ADCP velocity profiles, *J. Atmos. Oceanic Technol.*, *19*, 205–224.

Prandke, H., and A. Stips (1998), Test measurements with an operational microstructure-turbulence profiler: Detection limit of dissipation rates, *Auquat. Sci.*, *60*, 191–209.

Prandke, H., K. Holtsch, and A. Stips (2000), MITEC technology development: The microstructure-turbulence measuring system MSS, *EUR 19733 EN*, European Communities.

Ribbe, J., and P. E. Holloway (2001), A model of suspended sediment transport by internal tides, *Cont. Shelf Res.*, *21*(4), 395–422.

Rippeth, T. P., P. Wiles, M. R. Palmer, J. Sharples, and J. Tweddle (2009), The diapcynal nutrient flux and shear-induced diapcynal mixing in the seasonally stratified western Irish Sea, *Cont. Shelf Res.*, *29*(13), 1580–1587.

Sandstrom, H., and J. A. Elliott (1984), Internal tide and solitons on the Scotian shelf—A nutrient pump at work, *J. Geophys. Res.*, *89*(C4), 6415–6426, doi:10.1029/JC089iC04p06415.

Sandstrom, H., and N. S. Oakey (1995), Dissipation in internal tides and solitary waves, *J. Phys. Oceanogr.*, *25*(4), 604–614.

Sharples, J., C. M. Moore, and E. R. Abraham (2001a), Internal tide dissipation, mixing, and vertical nitrate flux at the shelf of NE New Zealand, *J. Geophys. Res.*, *106*(C7), 14,069–14,081, doi:10.1029/2000JC000604.

Sharples, J., C. M. Moore, T. P. Rippeth, P. M. Holligan, D. J. Hydes, N. R. Fisher, and J. H. Simpson (2001b), Phytoplankton distribution and survival in the thermocline, *Limnol. Oceanogr.*, *46*(3), 486–496.

Sharples, J., J. F. Tweddle, J. A. M. Green, et al. (2007), Spring-neap modulation of internal tide mixing and vertical nitrate fluxes at a shelf edge in summer, *Limnol. Oceanogr.*, *52*(5), 1735–1747.

Sherwin, T. J. (1988), Analysis of an internal tide observed on the Malin shelf, north of Ireland, *J. Phys. Oceanogr.*, *18*(7), 1035–1050.

Smith, W. H. F., and D. T. Sandwell (1997), Global seafloor topography from satellite altimetry and ship depth soundings, *Science*, *277*, 1957–1962.

St. Laurent, L., and R. W. Schmitt (1999), The contribution of salt fingers to vertical mixing in the North Atlantic Tracer Release Experiment, *J. Phys. Oceanogr.*, *29*(7), 1404–1424.

Stastna, M., and K. G. Lamb (2008), Sediment resuspension mechanisms associated with internal waves in coastal waters, *J. Geophys. Res.*, *113*, C10016, doi:10.1029/2007JC004711.

Vlasenko, V., and K. Hutter (2002), Numerical experiments on the breaking of solitary internal waves over a slope-shelf topography, *J. Phys. Oceanogr.*, *32*(6), 1779–1793.

H. Bange, P. Brandt, M. Dengler, and J. Schafstall, Leibniz-Institut für Meereswissenschaften, Düsternbrooker Weg 20, 24105 Kiel, Germany. (jschafstall@ifm-geomar.de)